46th AIAA/ASME/SAE/ASEE Joint Propulsion Conference & Exhibit, July 25-28, 2010, Nashville, Tennessee

Transient Three-Dimensional Side Load Analysis of Out-of-Round Film Cooled Nozzles

Ten-See Wang*, Jeff Lin†, Joe Ruf‡, and Mike Guidos§
NASA Marshall Space Flight Center, Huntsville, Alabama, 35812

The objective of this study is to investigate the effect of nozzle out-of-roundness on the transient startup side loads at a high altitude, with an anchored computational methodology. The out-of-roundness could be the result of asymmetric loads induced by hardware attached to the nozzle, asymmetric internal stresses induced by previous tests, and deformation, such as creep, from previous tests. The rocket engine studied encompasses a regeneratively cooled thrust chamber and a film cooled nozzle extension with film coolant distributed from a turbine exhaust manifold. The computational methodology is based on an unstructured-grid, pressure-based computational fluid dynamics formulation, and a transient inlet history based on an engine system simulation. Transient startup computations were performed with the out-of-roundness achieved by four different degrees of ovalization: one perfectly round, one slightly out-of-round, one more out-of-round, and one significantly out-of-round. The results show that the separation-line-jump is the peak side load physics for the round, slightly our-of-round, and more out-of-round cases, and the peak side load increases as the degree of out-of-roundness increases. For the significantly out-of-round nozzle, however, the peak side load reduces to comparable to that of the round nozzle and the separation line jump is not the peak side load physics. The counter-intuitive result of the significantly out-of-round case is found to be related to a side force reduction mechanism that splits the effect

* Aerospace Engineer, ER42, Fluid Dynamics Branch, Propulsion Structure, Thermal, and Fluids Analysis Division, Senior Member AIAA.
† Aerospace Engineer, ER42, Fluid Dynamics Branch, Propulsion Structure, Thermal, and Fluids Analysis Division,.
‡ Aerospace Engineer, ER42, Fluid Dynamics Branch, Propulsion Structure, Thermal, and Fluids Analysis Division.
§ Aerospace Engineer, ER21, Liquid Engine & Main Propulsion Systems Branch, Propulsion Systems Design & Integration Division.

of the separation-line-jump into two parts, not only in the circumferential direction and most importantly in time.

Nomenclature

C_1, C_2, C_3, C_μ= turbulence modeling constants, 1.15, 1.9, 0.25, and 0.09.

C_p = heat capacity

D = diffusivity

F_{yz} = integrated force in the lateral direction

H = total enthalpy

K = thermal conductivity

k = turbulent kinetic energy

L/S = ratio of long axis to short axis

Q = heat flux

T = temperature

t = time, s

u = mean velocities

V^2 = $\sum u^2$

x = Cartesian coordinates or nondimensional distance

α = species mass fraction

ε = turbulent kinetic energy dissipation rate

θ = energy dissipation contribution

μ = viscosity

μ_t = turbulent eddy viscosity ($=\rho C_\mu k^2/\varepsilon$)

Π = turbulent kinetic energy production

ρ = density

σ = turbulence modeling constants, 0.9, 0.9, 0.89, and 1.15 for Eqs. (2), (4)~(6).

τ = shear stress

ω = chemical species production rate

Subscripts

r = radiation

t = turbulent flow

w = wall

∞ = ambient

I. Introduction

Nozzle lateral forces during transient operations, if not properly managed, are known to cause severe structural damages to the engine and its supporting flight hardware to almost all liquid rocket engines during their initial development [1-4]. For example, the J-2 engine had its gimbal block retaining bolts failed in tension [4], the Space Shuttle Main Engine (SSME) had the liquid hydrogen feedline or steerhorn fractured [2,4], and the Japanese LE-7A engine had its cooling tubes broken [3]. And there have been many unreported incidents all over the world. Therefore, transient nozzle side load is always considered a high risk item and a critical design issue during any new engine development. For that reason, many research efforts [5-18] have been devoted to the understanding of the side load physics and its impact on the magnitude of side loads, to name a few.

The Area I upper-stage engine under development, the J-2X engine, is an evolved variation of two historic predecessors: the powerful J-2 engine that propelled the upper stages of the Apollo-era Saturn IB and Saturn V rockets, and the J-2S, a derivative of the J-2 that was developed and hot-fire tested but never flown, and both have seen the damaging nature of the side forces. It is therefore expected that the J-2X engine will experience side forces, just like its predecessors such as J-2 and J-2S [1], or engines similar in film cooling design such as the LE-7A [3, 13] and Vulcain engines. Tomita, et al. noted that the new design of LE-7A engine has given up the film cooling design - a source of the damaging peak side load physics, or the separation line jump [3, 8]. The impact of side forces on J-2X engine structures is therefore a major concern for the nozzle designers and test engineers, with good reasons.

To understand that impact on J-2X engine structures, a computational fluid dynamics (CFD) methodology [7, 8] has been used to study the J-2X side load under various operating conditions and environments, and to explore various possibilities during future tests and flights. One of the potential issues currently being explored is the effect

of nozzle deformation, or out-of-roundness of the nozzle. Liquid rocket engine nozzles, being large with relatively light weight structures, are probably never truly round. The causes of out-of-roundness could be, but are not limited to, the asymmetric loads induced by hardware attached to the nozzle, asymmetric material internal stresses induced in previous tests, and nozzle wall material deformation, such as creep, incurred in previous engine tests.

The current interest in the out-of-round nozzles comes from the fact that in perfectly round nozzle, nozzle side forces arise from asymmetric shock revolutions, questions were therefore raised about the side load characteristics of permanently deformed, out-of-round nozzle. To gain insight into side load characteristics of out-of-round nozzles, transient 3-D CFD analyses were performed on J-2X startup process. The nozzle out-of-roundness was achieved by assuming ovalized nozzles. In all, four nozzles with different degrees of ovalization were used to study the effect of out-of-roundness: a perfectly round nozzle or the baseline nozzle, a slightly ovalized nozzle, a more ovalized nozzle, and a significantly ovalized nozzle. To the best of authors' knowledge, this is the first attempt in studying the effect of nozzle out-of-roundness on side loads. Ostlund and Bigert [9] have studied several non-round, polygon nozzles. Those polygon nozzles are not out-of-round nozzles, however, because those were specially designed for the purpose of critical nozzle side load reduction. Finally, since J-2X is an upper stage engine, these transient computations were performed with a back pressure equivalent to 100,000 ft. The results of these computations are presented and discussed herein.

II. Computational Methodology

A. Computational Fluid Dynamics

The CFD methodology is based on a multi-dimensional, finite-volume, viscous, chemically reacting, unstructured grid, and pressure-based formulation. Time-varying transport equations of continuity, species continuity , momentum, total enthalpy, turbulent kinetic energy, and turbulent kinetic energy dissipation were solved using a time-marching sub-iteration scheme and are written as:

$$\frac{\partial \rho}{\partial t} + \frac{\partial}{\partial x_j}\left(\rho u_j\right) = 0 \tag{1}$$

$$\frac{\partial \rho \alpha_i}{\partial t} + \frac{\partial}{\partial x_j}\left(\rho u_j \alpha_i\right) = \frac{\partial}{\partial x_j}\left[\left(\rho D + \frac{\mu_t}{\sigma_\alpha}\right)\frac{\partial \alpha_i}{\partial x_j}\right] + \omega_i \tag{2}$$

$$\frac{\partial \rho u_i}{\partial t} + \frac{\partial}{\partial x_j}\left(\rho u_j u_i\right) = -\frac{\partial p}{\partial x_i} + \frac{\partial \tau_{ij}}{\partial x_j} \tag{3}$$

$$\frac{\partial \rho H}{\partial t} + \frac{\partial}{\partial x_j}\left(\rho u_j H\right) = \frac{\partial p}{\partial t} + Q_r + \frac{\partial}{\partial x_j}\left(\left(\frac{K}{C_p} + \frac{\mu_t}{\sigma_H}\right)\nabla H\right) + \frac{\partial}{\partial x_j}\left(\left((\mu + \mu_t) - \left(\frac{K}{C_p} + \frac{\mu_t}{\sigma_H}\right)\right)\nabla\left(V^2/2\right)\right) + \theta \tag{4}$$

$$\frac{\partial \rho k}{\partial t} + \frac{\partial}{\partial x_j}\left(\rho u_j k\right) = \frac{\partial}{\partial x_j}\left[\left(\mu + \frac{\mu_t}{\sigma_k}\right)\frac{\partial k}{\partial x_j}\right] + \rho\left(\Pi - \varepsilon\right) \tag{5}$$

$$\frac{\partial \rho \varepsilon}{\partial t} + \frac{\partial}{\partial x_j}\left(\rho u_j \varepsilon\right) = \frac{\partial}{\partial x_j}\left[\left(\mu + \frac{\mu_t}{\sigma_\varepsilon}\right)\frac{\partial \varepsilon}{\partial x_j}\right] + \rho\frac{\varepsilon}{k}\left(C_1\Pi - C_2\varepsilon + C_3\Pi^2/\varepsilon\right) \tag{6}$$

A predictor and corrector solution algorithm was employed to provide coupling of the governing equations. A second-order central-difference scheme was employed to discretize the diffusion fluxes and source terms. For the convective terms, a second-order upwind total variation diminishing difference scheme was used. To enhance the temporal accuracy, a second-order backward difference scheme was employed to discretize the temporal terms. Point-implicit method was used to solve the chemical species source terms. Sub-iterations within a time step were used for driving the system of second-order time-accurate equations to convergence. Details of the numerical algorithm can be found in Ref's [19-22].

An extended k-ε turbulence model [23] was used to describe the turbulence. A modified wall function approach was employed to provide wall boundary layer solutions that are less sensitive to the near-wall grid spacing. Consequently, the model has combined the advantages of both the integrated-to-the-wall approach and the conventional law-of-the-wall approach by incorporating a complete velocity profile and a universal temperature profile [24]. A 7-species, 9-reaction detailed mechanism [24] was used to describe the finite-rate, hydrogen/oxygen afterburning combustion kinetics. The seven species are H_2, O_2, H_2O, O, H, OH, and N_2. The thermodynamic properties of the individual species are functions of temperature. The multiphysics pertinent to this study have been anchored in earlier efforts, e.g., SSME axial force and wall heat transfer [19], SSME startup side load and dominant shock breathing frequency [7], J-2X startup and shutdown side loads for a nozzlette configuration [8], nozzle film cooling applications [25], and conjugate heat transfer [26].

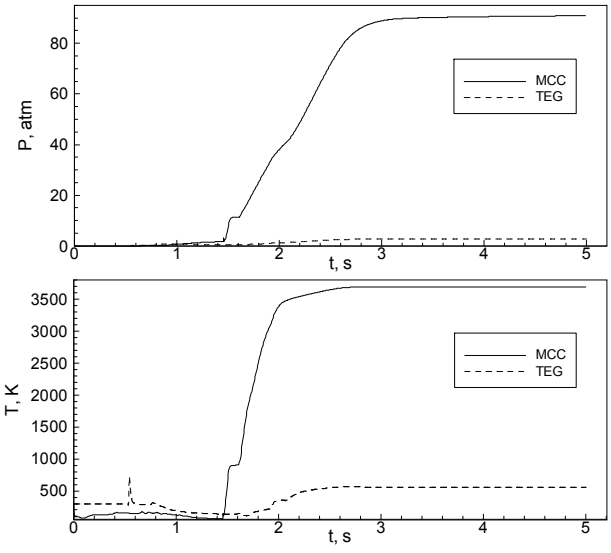

Fig. 1 Simulated inlet pressure and temperature histories for the main combustion chamber and turbine exhaust gas flows during the start-up transient.

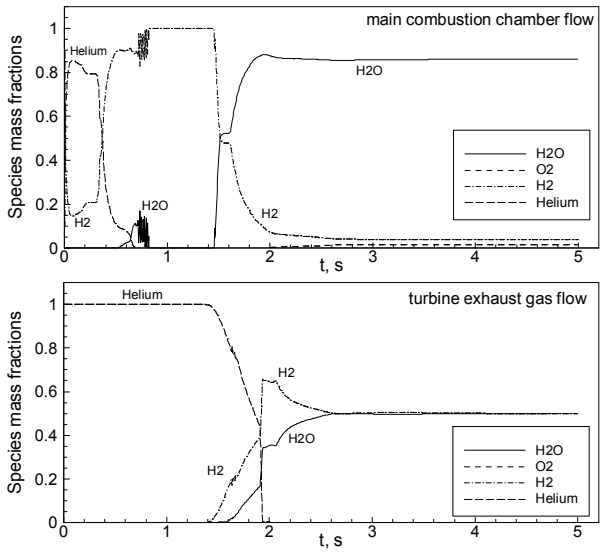

Fig. 2 Simulated inlet species mass fraction histories for the main combustion chamber and turbine exhaust gas flows during the start-up transient.

C. Transient Startup Sequences

The startup and shutdown sequences are very important drivers to the nozzle side load physics [7, 8]. They contain not only the inlet pressure and temperature histories, but also the species mass fraction histories. The ramp rate of the pressure sequence generally determines the magnitude and duration of the peak side load. The temperature and species mass fraction sequences determine the extent of the combustion reactions that in turn affects the magnitude and duration of the peak side load. Another reason the temperature and species composition are important is because they largely determine the specific heat distribution which in turn determine the shock shape, which again impacts the side load physics. Given another example of the importance of the species composition, if excess fuel is dumped at certain period of time, combustion waves could occur and that add to the severity of the side load [7].

Transient system-level simulations provide the histories of the aforementioned variables as determined from a lumped, control-volume analysis approach to simulate the network of components and sub-components, including the valve actions, in a rocket engine. Transient system-level modeling is therefore an important tool in the design and planning of sequencing the transient events of rocket engine operation. In our case, it is also an important tool for nozzle aerodynamic design and the subsequent analysis for test stand operations. Figure 1 shows the inlet

pressure and temperature histories, and Fig. 2 shows the inlet species mass fraction histories, for the main combustion chamber (MCC) and the turbine exhaust gas (TEG) flows during the startup transient for this study. TEG flow is used as film coolant for the J-2X engine nozzle extension as well as providing a small benefit to engine thrust performance. The transient reactant composition obtained from system modeling at the two inlets was preprocessed with the Chemical Equilibrium Calculation program [27], assuming the propellants were ignited to reach equilibrium composition immediately beyond the injector faceplate or inlet boundary. It can be seen from Fig. 1 that the MCC pressure and temperature ramps mainly between 1.4 and 3 s. Also, it can be seen from Fig. 2 that immediately following the start command, helium gas enters both the MCC, via purge flow, and the TEG chamber, initially via purge flow but then as flow injected to assist the start-up of the J-2X turbopumps.

Helium is initially present in the MCC-nozzle flowfield due to purges used during the early stages of the start sequence from the main injector and Gas Generator (GG) TEG flowpath. This helium in the MCC is pushed out as the initial fuel flow and igniter low-flow/low-pressure combustion flows become established to the MCC, as shown in the transient MCC species mass fraction profile in Fig. 2. The main fuel valve is opened first, to establish the initial fuel flow in the main fuel injector and MCC augmented spark igniter (ASI), ensuring a fuel-rich start of the MCC and safely allowing the J-2X fuel turbopump to start ramping up. To provide the initial break-away momentum to the pumps and initiate higher pump flow-rates, a helium spin-assist system is used to inject a short-duration (~1.4 sec), high pressure/high-flow of helium gas into the turbines. Simultaneous with the initiation of the helium-spin assist system, the main oxidizer valve is opened to allow priming of the downstream oxidizer system with purely liquid oxidizer. Also in this same period, the low-flow oxidizer valve is opened to allow flow to the MCC ASI and initiate low-flow/low-pressure combustion in this early timeframe. It is during this ~1.4 sec interval of spin-system operation, and prior to any significant flow through the MCC main injector, that the nozzle side-loads peak (at 0.80-1.10 sec).

As the spin-start system is initiated, the helium is exhausted through the TEG flowpath, (after passing through the fuel and oxidizer turbines) and into the nozzle flowfield. As already mentioned, this discharge of helium-spin gas from the TEG into the nozzle flow-field occurs prior to any significant flow through the main injector, thus promoting the possibility of loading of the nozzle asymmetrically. As the TEG flow decays, the GG fuel and oxidizer valves are opened, and the flows are combusted in the GG, further accelerating the pumps and both fuel and oxidizer flows throughout the engine. However, this transition of pump-driving fluid, from spin-assist helium to

GG-generated hot gas is not instantaneous, and there is a time delta that occurs during which engine system flows and pressures decay.

During this power-transition period, the main injector oxidizer dome primes with liquid oxygen, which is a crucial step in starting the engine safely, as the oxidizer flow to the MCC then becomes more controllable and predictable, increasing the likelihood for stable MCC combustion as engine power is sharply increased. As the flow of oxidizer in the main oxidizer injector initiates and then primes with liquid, the MCC pressure rises sharply to the first small plateau in the ~1,4-1.6 sec timeframe as shown in the transient MCC pressure profile in Fig. 1. The rise in MCC pressure correspondingly causes a decrease in fuel system flow and pressure to the MCC, thus causing the brief stagnation or plateau in MCC pressure.

Once the GG combustion flow begins to build (which exhausts through the TEG flowpath), the pumps accelerate, and their respective propellant flows to the MCC also accelerate, driving the engine system to full power (or mainstage) conditions throughout. After the start of the GG and the hot combustion gas flow rapidly builds, the remaining helium in the TEG flowpath is completely pushed out, as shown in the transient TEG species mass fraction profile in Fig. 1. Essentially, engine steady-state operation is attained approximately within 4.5 to 5.0 sec after engine start command is received, although thermal equilibrium effects between the propellant flows and the metal mass within the engine prevent flows from completely steadying until a much later time.

These helium flows effectively dilute the fuel concentration in the early startup process. It was found in an earlier study [8] that a combination of the fuel dilution and a shorter ramp time than that of the SSME eliminated the occurrence of potentially hazardous combustion wave [7]. It is noted that the startup sequences shown in Figs 1 and 2 are different from those shown in an earlier study [8], e.g., the temperature spike during the earlier startup transient [8] was eliminated based on revisions to the J-2X valve sequencing.

III. Computational Grid Generation

The computational domain for the J-2X out-of-round nozzle side load investigation includes the MCC, nozzle, turbine exhaust manifold (TEM), nozzle extension, plume, and freestream regions. Since the current thruster model includes a TEM, it is called a TEM configuration, in contrast to that of the nozzlette configuration used in an earlier study [8]. Both the nozzlette [8] and TEM are used to supply film coolant, or TEG, to the nozzle extension. The difference between the two configurations is that nozzlette geometry is symmetric to the thruster centerline, implying a uniform mass flow distribution in the circumferential direction; while the TEM is essentially a torus which is not symmetric to the thruster centerline, implying a non-uniform mass flow distribution circumferentially. Figure 3 shows a typical grid layout of the nominal or perfectly round thruster with the current TEM configuration. The TEM consists of an inlet duct and an aforementioned torus with which the incoming TEG flow is split under the inlet duct, flowing around the torus and entering the nozzle extension. The torus has a tapered flow area from just under the inlet duct all the way to the opposite end. The tapered flow area was intended for a near uniform film coolant flow distribution when TEG enters the nozzle extension. However, for this particular TEM configuration, a separate steady-state analysis indicated a +9% variation in mass flow distribution from the inlet duct side to the opposite side of the torus during main stage.

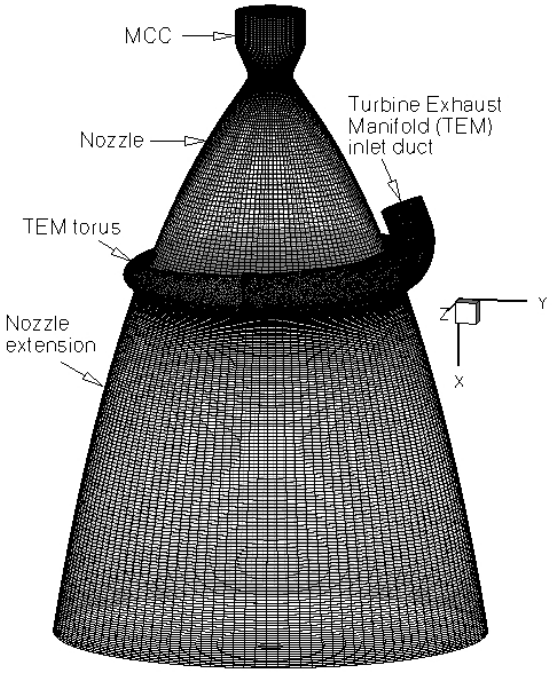

Fig. 3 A grid layout of the nominal thruster.

The general procedure of the grid generation follows that of the SSME side load study [7] and nozzlette configuration of J-2X side load study [8] by rotating an axisymmetric grid first without the TEM. The TEM grid was constructed separately as it is asymmetric to the central axis. The final grid was completed by merging these two grids at the interface. A software package GRIDGEN [28] was used to perform the grid generation. The general layout of the outer boundaries and the wall boundaries of the MCC, nozzle, TEM, and nozzle extension are similar to those of the nozzlette configuration, which is described in detail in Ref. [8] and is not repeated in here. Figure 4 shows a close-up view of the MCC, nozzle, and TEM without the nozzle extension attached to the perfectly round nozzle. It can be seen that the turbine exhaust gas flow comes in from the TEM inlet duct, splits under the inlet duct and flows around the TEM torus and over the structural ribs, and finally entering the nozzle extension through the TEG exit ring as a protective barrier between the hot core flow and the nozzle extension.

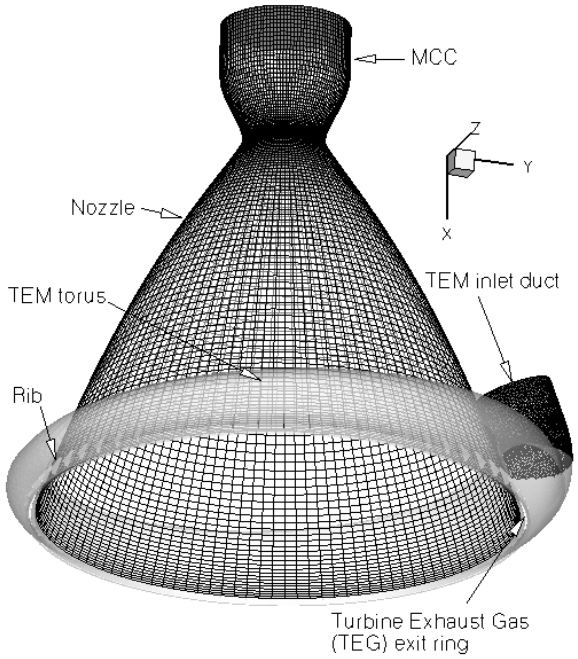

Fig. 4 A close-up view of the turbine exhaust manifold of the nominal thruster.

A grid study procedure was developed for transient nozzle side load calculations in earlier studies [7, 8, 19]. It was based on the recognition that a conventional grid study is computationally prohibitive for side load investigations because of the need for large amount of computer resources, due to the requirements of full 360 degrees of three-dimensional domain, turbulent reacting flow, and integration of 3 to 5 s of transient operational times. Knowing that peak side force is usually a small percentage of the axial force, the grid study is performed on a steady-state axial force calculation, based on the assumption that if the grid density is adequate for the calculated steady-state axial force, then it is adequate for the calculated transient side forces. The grid study starts with the axisymmetric grid first, then the 3-D grid next. The 3-D grid is achieved by rotating the axisymmetric grid 360 degrees to ensure the asymmetric flow come from the transient physics and not the asymmetric grid. It is critical that the grid density for the axisymmetric grid is adequate. Otherwise the rotated 3-D grid will have a difficult time matching the desired axial force [19]. From the results of previous studies

on the transient startup of the SSME, and the transient startup and shutdown of the nozzlette J-2X engine, a circumferential division number of 72 was found to be adequate in capturing all the major side load physics such as the shock transitions, shock breathing across the nozzle lip, and separation line jump, and the side load computed for those major physics agreed reasonable well with those of the hot-fire test measurement [7, 8]. In addition, the computed dominant oscillation frequency during the shock breathing also agreed well with test measurement [7]. This grid study procedure is therefore demonstrated to be efficient for nozzle side load study.

In this effort, due to increased computational resources, the circumferential division number is increased to 120, or a 67% increase over the previous efforts [7, 8]. To test the effect of the increased circumferential grid resolution, a separate transient startup calculation of the J-2X stub nozzle at sea level was performed to see if teepees can be captured. Teepees are formations of conical shocks that occur near the nozzle lip and observed during sea level hot-fire tests. It is first described by Nave and Coffey [1] during J-2S engine tests and is often observed during SSME startup transients as well. It usually occurs during the shock breathing mode [7] when the shock foot comes in and out of the nozzle lip. A stub nozzle without the nozzle extension is chosen because a shorter nozzle flows full faster. The result in reduced Mach number contours show that shock breathing occurring between 1.775 ~ 1.94 s and teepees are seen between 1.775 ~ 1.845 s. Figure 5 shows clearly captured teepees with separation and reattachment lines at 1.82 s into the startup transient. The total number of teepees captured in this time slice is thirteen, which is much improved over the three to five teepee-like structures captured in previous studies [7, 8]. This result shows one aspect of improvement in capturing the transient nozzle physics through the increased circumferential grid resolution.

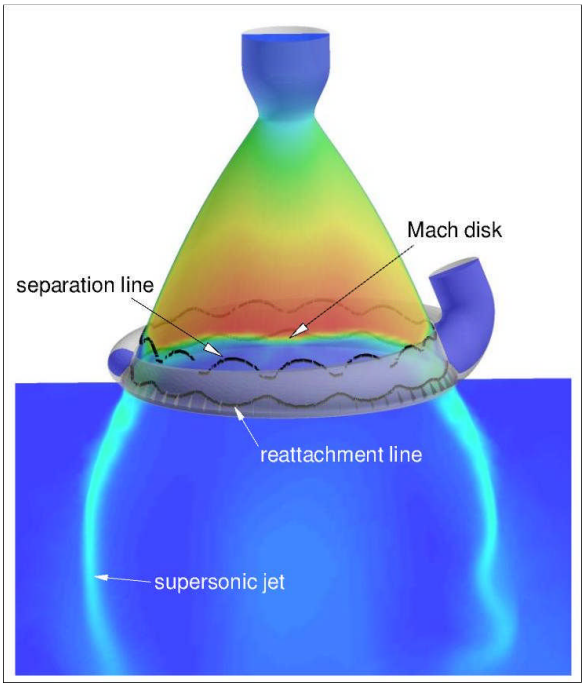

Fig. 5 Separation, reattachment lines and .Mach number contours for a nominal stub nozzle at 1.82 s into startup transient at sea level

For out-of-round nozzles, the out-of-roundness is achieved by ovalizing the thruster, or by varying the ratio of the long axis to the short axis or L/S, from the perfectly round thruster. Figure 6 shows a cross-sectional view of the

four thrusters generated for this study. The nominal, or the perfectly round case, has a L/S ratio of unity; the slightly out-of-round case, has a L/S ratio of 1.0086; the more out-of-round case, has a L/S ratio of 1.0346. Finally, the L/S ratio of the significantly out-of-round case is a hypothetically high at 1.4400. It is estimated that the slightly out-of-round and the more out-of-round cases are the most likely scenarios of previously mentioned internal stresses, while the significantly out-of-round thruster is intended as a hypothetical case that serves as the worst or the most conservative case. That is, the effect of out-of-roundness on nozzle side load physics might be drastically magnified with the significantly out-of-round nozzle.

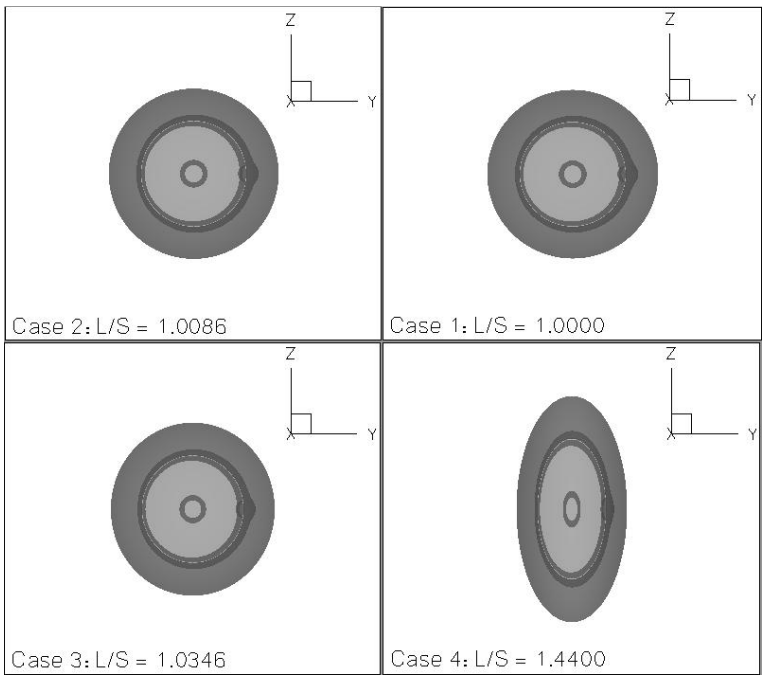

Fig. 6 Cross-sectional view of the ovalized nozzles.

Due to the nature of the TEM structure and other available information, it is assumed that the long axis is aligned with the z-coordinate. The short axis is therefore aligned with the y-coordinate, as indicated in Fig. 6. The total number of grid points is 3,653,299, or 4,421,166 cells for all four cases. The total cell numbers used in this study is higher than the 2,058,192 cells used in the nozzlette configuration study [8], and much higher than the 1,275,120 cells used in the SSME benchmark [7]. It is noted that although the cross-sectional flow areas of the four thrusters do not have to be the same, it is further assumed that those are the same such that the results are compared on an equal flow area basis.

IV. Boundary and Inlet Conditions

Since J-2X is the upper stage engine of the Area I vehicle, fixed total conditions were used for the freestream boundaries with those corresponding to 100,000 ft. Time-varying inlet flow boundary conditions were used at the inlets for the MCC and TEG flows. These time-varying inlet flow properties were obtained from the system-level

simulations that include the time varying total pressure, temperature, and reactant composition, as shown in Figs. 1 and 2. The details about the system-level simulations are discussed earlier. For startup computations, the thermal wall boundary condition was started out as adiabatic. As the startup transient reaches 1.4 s, when the MCC pressure starts to ramp up, wall temperature profiles obtained from separate steady-state calculations were imposed onto the thruster walls, as discussed in [7, 8].

V. Results and Discussion

The computations were performed on a cluster machine using 10~15 processors. For sea level transient computations [7, 8], global time steps were varied throughout the computations: 2.5~10 μs were typically used during the initial transient when the change of flow physics was mild, and 1~2.5 μs were used when strong flow physics such as combustion, shock transitions and separation line jump were occurring. For transient computations at 100,000 ft, since the combustion reaction rate at such an altitude is much slower than those at sea level, a fixed global time step of 10 μs was used throughout the computations. These global time steps used correspond to CFL numbers ranging approximately from 0.1 to unity. The run matrix of the four cases is shown in Table 1. The result of the nominal case will be discussed first, followed by those of the three out-of-round cases.

Table 1 Run matrix

Case	Description	L/S ratio	Deformation, in
1	Nominal or perfectly round	1.0000	± 0.00
2	Slightly out-of-round	1.0086	± 0.25
3	More out-of-round	1.0346	± 1.00
4	Significantly out-of-round	1.4400	± 11.6

A. The Nominal Case

Figure 7 shows the computed J-2X side load history during startup transient for the perfectly round case. Major startup physics and the timeline of their occurrence and duration are indicated at the top of the figure. A brief description of the time evolving physics is therefore in order. As shown in Fig. 7, the exhaust plume of the transient startup begins as a subsonic core jet. As the chamber pressure increases, the core jet flow strengthens. When the core jet becomes supersonic, a Mach disk develops near the throat at around 0.40 s. Due to wall friction, this initial Mach disk flow is separated from the nozzle wall from the throat down. The combination of this flow separation pattern and the associated shock structure of the Mach disk flow is named as the free-shock separation (FSS) [1], because the supersonic jet stemming from the triple point is flowing freely away from the wall. As this Mach disk flow advances downstream, the size of the Mach disk grows as the nozzle flowing area increases. At about 0.65 s into the transient process, the TEG flow emerges from the TEG exit ring.

As described earlier, this TEM configuration implies a +9% variation in mass flow distribution circumferentially from the inlet duct side to the opposite side during the main stage. However, during the early startup transient, more

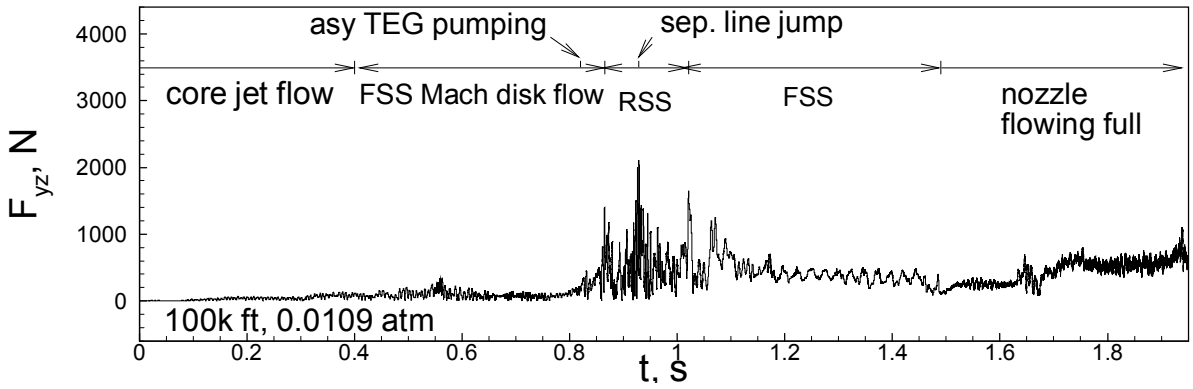

Fig. 7 Computed side load history during startup for the nominal or perfectly round case.

TEG flow comes out from TEG exit ring under the TEM inlet duct, producing a pumping effect. In addition, since the ambient pressure at 100k ft is lower than that of the total pressures of the core and TEG flows, the external environment also behaves like a vacuum pump. These pumping effects exercibate the TEG flow imbalance which draws the supersonic jet towards the TEM inlet duct side, forming an asymmetric Mach disk flow with a slanted separation line, as shown in the snapshot at 0.85 s in Fig. 8. This phenomenon is unique to this TEM configuration during startup and is named as the "asymmetric TEG pumping" herein. As a result, this phenomenon helps the asymmetric FSS Mach disk flow transiting into an asymmetric Restricted-Shock Separation (RSS) Mach disk flow, generating the first local peak side load at about 0.865s, as indicated in Fig. 7. At 0.86 s in Fig. 8, the supersonic jet

is merging with the TEG flow, forming a RSS flow pattern. With a RSS flow pattern, all part of the supersonic jet is attached or restricted to the nozzle wall, and it was first observed and reported during J-2 and J-2S tests [1].

At this time, the rear shock stem is fast approaching the setup of TEG exit ring which composes of a small "base', or a back-step formation between the nozzle contour and the TEG exit ring. As one can expect from intuition, when the rear shock stem finally jumps over a cliff, or the base, and then meet with a flowing TEG flow, a significant disturbance is imposed onto the Mach disk flow. At 0.92 s, Fig. 8 shows the shock stem of the RSS Mach disk flow just before the jump. At 0.929 s into the startup transient, the rear shock stem, or the separation line, jumps over the TEG exit ring setup and a peak side load of 2114 N is generated. This separation line jump phenomenon was first reported by Watabnabe [3] as "separation point jump" during LE-7A engine tests. Later Wang [8] captured it computationally with a J-2X nozzlette configuration. Since the separation line jump always produces a peak side load, it is considered as the critical side load physics for regular, round, film cooled nozzles. Tomita, et al noted that back-step formation exaggerates the effect of separation line jump [29]. The 0.93 s snapshot in Fig. 8 shows a disturbed Mach disk flow right after the jump. After that the Mach disk flow continues its downstream movement, as shown in the 1.0 s snapshot. Subsequently, the RSS Mach disk flow transits back to a FSS Mach disk flow at about 1.01 s, generating another local peak side load. This FSS Mach disk flow oscillates several more times in the nozzle and eventually leaves the nozzle at around 1.49 s.

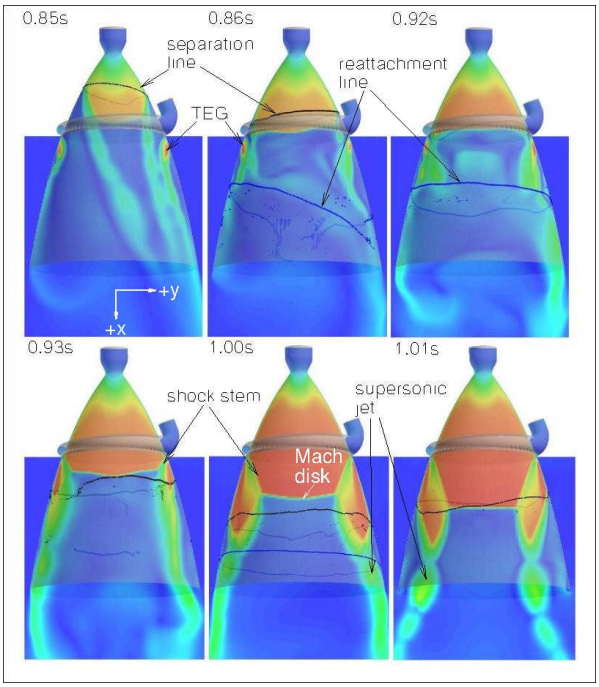

Fig. 8 Mach number contours on xy-plane at selected time slices for the nominal case.

B. Out-of-round Cases

Since nozzle side forces are caused by asymmetric flows, or specifically, asymmetric shock formations caused by major side load physics during the transient process, e.g., combustion wave, FSS-to-RSS transition and vice

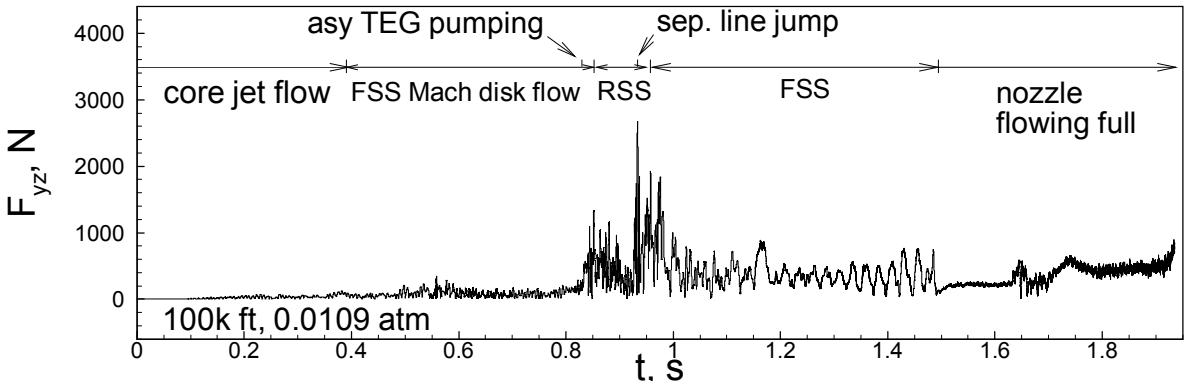

Fig. 9 Computed side load history during startup for the slightly out-of-round case (L/S = 1.0086).

versa, shock breathing at the lip, and jump of the separation line, it is anticipated that any further changes in operation or configuration that causes asymmetric flow, exercibate the situation. As a case in point, the biased TEG flow distribution due to the current TEM configuration is an example of configuration change that promotes the asymmetric TEG pumping, resulting in more severe asymmetric shock formation, and higher peak side load than that of a nozzlette configuration. Nozzle out-of-roundness, conceptually, is another form of configuration change. Hence, it is expected that higher degree of out-of-roundness, measured by the ratio of length of long axis to that of short axis in this study, could lead to higher peak side load.

Figure 9 shows the computed side load history and the timeline of the major physics for the slightly out-of-round case. With a small L/S ratio of 1.0086, or a ± 0.25 in. deformation, this is the mostly likely case of permanent nozzle deformation due to internal stresses accumulated in previous tests, or due to asymmetric loads induced by other hardware attached to the nozzle. Since the out-of-roundness is quite small, it is expected that all the major side load physics occurring in the nominal case also happening in the slightly out-of-round case, for example, asymmetric TEG pumping, FSS-to-RSS transition, separation line jump, and RSS-to-FSS transition. The major physics indicated in Fig. 9 showed just that. More importantly, the peak side load is also caused by the jump of the separation line. With a magnitude of 2688 N, it is a 26% increase from that of the nominal case.

Figure 10 shows the computed side load history and the associated major physics for the more out-of-round case. With a little bigger L/S ratio of 1.0346 and a ± 1 in. physical deformation, such an out-of-roundness is still a likely

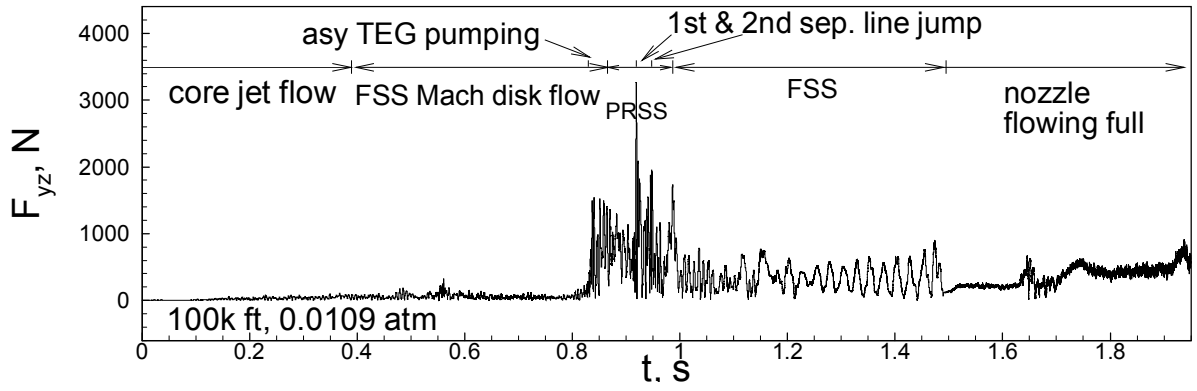

Fig. 10 Computed side load history during startup for the more out-of-round case (L/S = 1.0346)

scenario when the internal stress built up through many hot-fire tests. By comparing the major physics indicated in Fig. 10, with those of Figs. 7 and 9, it can be seen that all the major physics are still intact. Other than there are two differences between this case and the nominal and slightly out-of-round cases. First, after the asymmetric TEG pumping, instead of FSS-to-RSS transition, we now have a FSS-to-partial RSS (PRSS) transition. Second, instead of having one separation line jump, the current case has two separation line jumps. PRSS is a Mach disk flow separation pattern between that of a FSS and a RSS Mach disk flow patterns. That is, the supersonic jet is only partially attached to the nozzle wall. PRSS was first captured computationally in the unsteady simulations of LE-7, LE-7A, and CTP50-R5-L nozzles by Wonezawa, et al [30] and later on captured by Wang [7] in his transient startup computation of a SSME nozzle.

These differences may be explained by examining time slices of Mach number contours in Fig. 11. For each time slice, two pictures are shown. The picture on the left-hand-side is the Mach number contours on the xy-plane, while that on the right-hand-side is the Mach number contours on the xz-plane. The xy-plane view is associated with the short-axis side of the ovalized nozzle, while the xz-plane view is associated with the long-axis side of the ovalized nozzle. That association may not be obvious in this case, since a deformation of ± 1 in is still difficult to be picked up by naked eyes, but it will be obvious in the significantly out-of-round case to be examined later. At 0.83 s into the startup transient, as shown with the first time slice, the supersonic jet of the FSS Mach disk flow is feeling the effect of pumping from the TEG flow.

At 0.85 s into the startup transient, the supersonic jet merges with the TEG flow to become a PRSS Mach disk flow. The xy-plane and xz-plane views show that the supersonic jet is swaying to the quadrant of the TEM inlet duct side. The first separation line jump happens at around 0.91916 s. The disturbance to the Mach disk flow generates a peak side load of 3275 N, a 55% increase over that of the nominal case, as indicated in Fig. 10. The aftermath of that disturbance can be seen from the pictures at 0.925 s, where we have disturbed separation and reattachment lines, along with wildly swaying supersonic jet. In addition, the disturbance is so large that the rear shock stem retracted back above the TEG inlet ring, as shown from the partial and asymmetric separation line at 0.94 s. The partial reattachment line is also quite messy. That sets up the second separation jump at 0.94818 s. The magnitude of the local peak side load resulting from the second separation jump is lower at 1960 N, as expected. At 0.97 s, the PRSS Mach disk flow still feels the effect of second separation line jumps, with fairly irregular separation and reattachment lines. The PRSS then transits to FSS at 0.98652 s and generated a local peak side load of 1733 N. After that transition the Mach disk flow finally returns to normal, as indicated by the snapshot taken at 1.0 s.

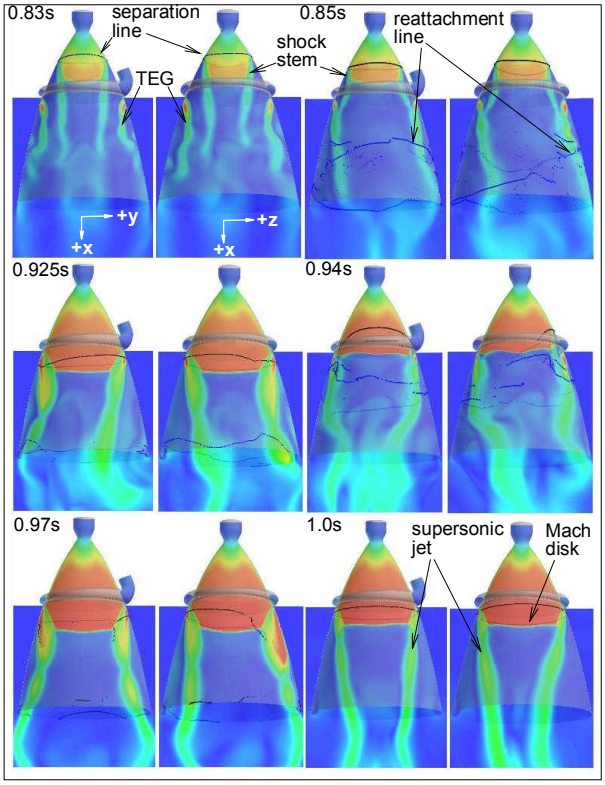

Fig. 11 Mach number contours at selected time slices for the more out-of-round case.

So far, with the increased degree of out-of-roundness and the resulting enhanced asymmetric flow, the progressively increased peak side loads for the slightly and more out-of-round cases from that of the nominal case are behaving as expected. One might expect the peak side load of the significantly out-of-round case would follow that same trend and increase significantly more than that of the nominal and other two out-of-round cases. Instead, the computed peak side load for the significantly out-of-round case turns out to be only slightly higher than that of the nominal case, as shown in Fig. 12. In addition, the peak side load is not generated from the normal peak side load physics of separation line jump, but from FSS-to-RSS transition.

This counter-intuitive result may again be explained by snapshots of the computed major side load physics using Mach number contours, as shown in Fig. 13. As presented earlier in Fig. 11 for the more out-of-round case, with each time slice, two views are shown: one for the xy-plane and another for the xz-plane. It is now obvious that xy-plane view shows the contours at the short-axis side, while the xz-plane view shows those at the long-axis side, due to the exaggerated ovalization. At 0.7 s into the startup transient, or the first two pictures on the upper left corner, one can see that on the xy-plane, the TEG flow under the inlet duct side appears to be equal in size as that of the opposite side. On the other hand, on the xz-plane, the TEG flow on the +z-coordinate side appears to be twice as big as that of the opposite side. The supersonic jet on the xy-plane therefore flows straight, while the supersonic jet on the xz-plane is swaying to the stronger pumping side. It can also be seen that the nozzle wall is much closer to the Mach disk flow in the xy-plane side than that of the xz-plane side. According to Coanda effect [7, 31], the jet is always attracted to the closer wall. Hence the supersonic jet on the xy-plane side is flowing closer to the wall and appears to be fatter, and the Mach disk appears to be bigger and advances a little bit further downstream; while the supersonic jet on the xz-plane side is too far away from the wall to have any Coanda effect, therefore it looks thinner, and the Mach disk is smaller and travels less distance downstream. Since the supersonic jet also pumps the TEG flow, it is speculated that a slight imbalance in the beginning may have temporarily directed more TEG flow to

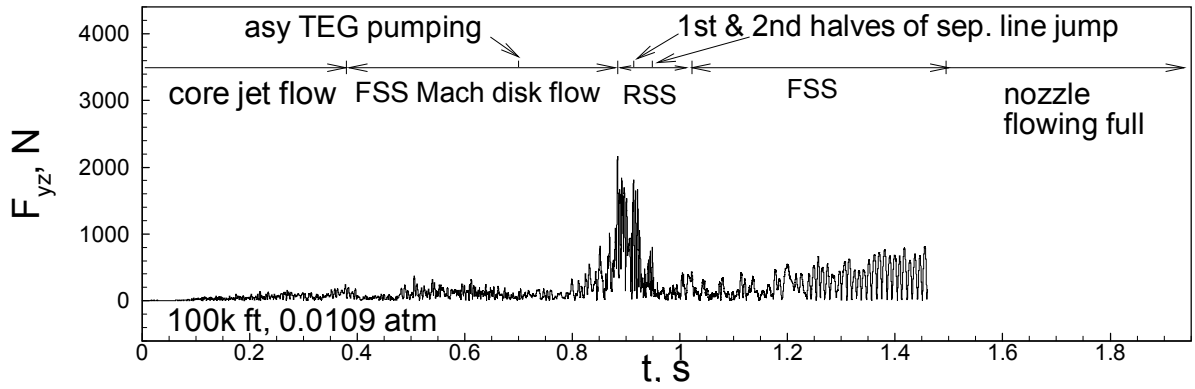

Fig. 12 Computed side load history during startup for the significantly out-of-round case (L/S = 1.4400)

the +z-coordinate side, hence the asymmetric TEG pumping on the longer, thinner supersonic jet in the xz-plane.

Another phenomenon worth emphasizing is that since the nozzle geometry is crashed on the xy-plane, and extending far and wide from side to side on the xz-plane, the shape of the separation line is no longer circular, but a sickle shape that bends downward on both ends of the short axis, as shown in the 0.7 s snapshot in Fig. 13. This is

clearly due to the Coanda effect therefore the shock stem advances further downstream on the two ends of the short-axis side. On the other hand, the shock stem travels less on the two ends of the long-axis side, due to a lack of Coanda effect. Note that the valley point of the sickle on the xz-plane is not on the centerline, but biased towards the bigger TEG flow side, affected by the right-swaying movement of the supersonic jet. The sickle-shaped initial separation line sets up a series of follow-up events that changed the peak side load physics of this case from those of the previous three cases.

Next, the FSS Mach disk flow transits to PRSS Mach disk flow at around 0.88 s. That disturbance moves the originally upward-bending sickle cell on the –z-coordinate side downward, thus severely distorted the Mach disk shape on the xz-plane, as shown in Fig. 13. This shock transition generates a peak side load of 2171 N. Note that the Mach disk shape on the xy-plane appears to be stable and not disturbed, due to the stabilizing Coanda effect. The flow separation pattern of the Mach disk flow switches between the PRSS and RSS from this time on. A RSS Mach disk flow is shown at 0.91 s into the startup transient, right before the first separation line jump. Note the shock stem on the xy-plane is much closer to the TEG inlet ring than that on the xz-plane.

There are two local side load peaks due to two separation line jumps, as shown in Fig. 12. Or to be technically correct, two halves of on separation line jump. The first half of the separation line jump occurs at 0.913875 s and generated a local peak side load of 1814 N, lower than that of the peak side load of 2171 N due to FSS-to-PRSS transition. The Mach number contours at 0.915 s is shown in Fig.13, right after the occurrence of the first half of the separation line jump. It can be seen that the separation and reattachment lines and the Mach disk on the xz-plane from those of 0.91 s are disturbed after the jump. Note there are two separation lines shown in the 0.915 s snapshot, the lower one formed by the TEG flow

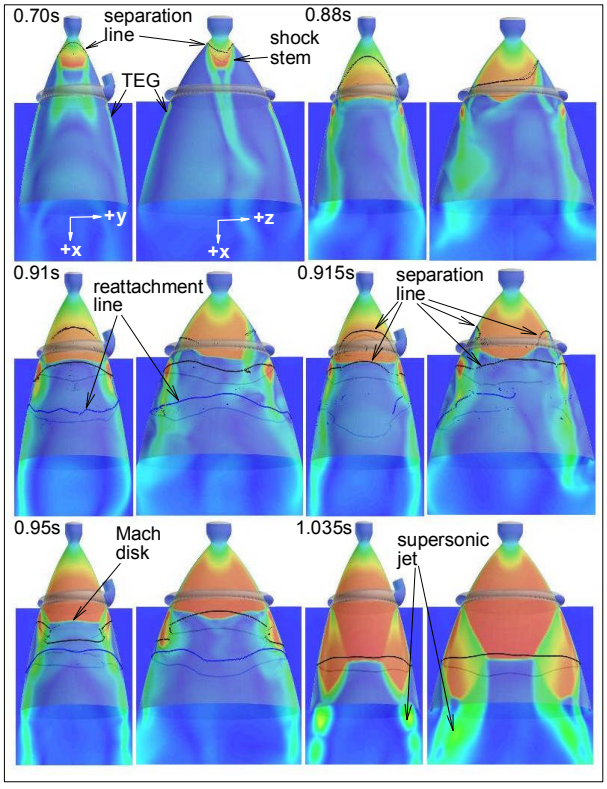

Fig. 13 Mach number contours of selected time slices for the significantly out-of-round case.

does not count since it never jumped. It is the part associated with the two ends of the upper separation line on the xy-plane that has jumped, whereas the part or two ends of the upper separation line on the xz-plane is still way above the TEG inlet ring, as shown in the 0.915 s snapshot in Fig. 13. The second half of the separation line jump, or the rest of the upper separation line on the two ends of xz-plane, happens at 0.94883 s and generates a local peak side load of 806 N. It is much lower than that of the first half of the separation line jump, because by this time, most of the upper separation line has already passed the TEG exit ring. The Mach number contours at 0.95 s into the startup transient, shown in Fig. 13, illustrate a more stable RSS flow pattern occurring right after the second half of the upper separation line jump, although the separation and reattachment lines still look irregular after that event. Note that the upper separation line that jumped disappears, because by this time, the rear shock stem has merged with the TEG flow and the upper flow separation zone is eliminated. The RSS to FSS transition occurs at 1.02223 s, which generated a small local peak side load of 436 N. That transition is the last of the major side load physics. After that, Fig. 13 shows a much stable Mach number contours at 1.035 s into the startup transient. The Mach disks on both planes look normal, and the separation lines finally appear to be closer to the regular shape.

Table 2. A comparison of the computed peak side loads

Nozzle shape	Peak Fyz, N	physics
perfectly round	2114	separation line jump
Slightly out-of-round	2668	separation line jump
More out-of-round	3275	separation line jump
Significantly out-of-round	2171	FSS-to-PRSS transition

A comparison of the peak side loads along with the associated side load physics is shown in Table 2. In Summary, the peak side load increases progressively with the slightly and more out-of-round cases during the separation line jump. However, there is a surprising side force stabilizing effect found during the transient startup of the significantly out-of-round case. It is attributed to the Coanda effect that helps the separation line moving downstream faster in the two ends of the xy-plane than those in the xz-plane, resulting in a sickle-shaped separation line at the beginning. The end result is that the normally peak side producing physics or separation line jump for the perfectly round, slightly out-of-round, and more out-of-round cases is now weakened by splitting into two parts. The fast moving part of the separation line that associated with the two ends of the short-axis side jumps first, and then the slow moving part of the separation line that associated with the two ends of the long-axis jumps second. This

splitting of the separation line jump is responsible for the peak side load reduction of the significantly out-of-round case.

As mentioned earlier, Ostlund and Bigert tested several non-round, or polygon nozzles at sea level [9]. The goal of the polygon nozzle design was to have a side load reduction of the first-side load peak, stemming from the transition between FSS and RSS, relative to a normal, round nozzle. The transition between FSS and RSS is said to be the critical side load physics for Vulcain-type nozzles. They reported that the goal was achieved after 10 tests and attributed the reduction to three possible mechanisms. One mechanism that is relevant to this study is that the polygon corners act as a kind of structure-breaker, leading to splitting of the separation of the flow pattern in the circumferential direction, hence the side load reduction. Hence, although the peak side load physics appear to be different between the J-2X and Vulcain type of nozzles, the mechanism that breaks the trend of progressively increasing side load with the increasing significantly out-of-round nozzle, is similar to that of the polygon nozzle with which the side load is reduced. That is, the splitting of the flow separation (separation line) is the mechanism responsible for the reduction of side load for the out-of-round J-2X nozzle and the non-round polygon nozzles. For the significantly our-of-round nozzle, however, the effect of the would-be peak side load physics is not only split in the circumferential direction, but also split in time. That is because the elapsed time between the two jumps is a prolonged 0.03496 s.

VI. Conclusion

Three-dimensional numerical investigations on the effect of nozzle out-of-roundness on side loads during transient startup process for a film cooled nozzle have been performed. Four cases of nozzle our-of-roundness have been computed for a nominal, perfectly round nozzle, a slightly out-of-round nozzle, a more out-of-round nozzle, and a significantly out-of-round nozzle. It is found that the separation line jump is the peak side load physics for the round, slightly our-of-round, and more out-of-round cases, and the peak side load increases as the degree of out-of-roundness increases. For the significantly out-of-round case, however, a surprising side force stabilizing effect is discovered. That side force stabilizing effect is caused by the Coanda effect working on a nozzle crashed in one direction and extending far and wide from side to side in another direction. Consequently, the sickle-shaped separation line on the two ends of the short-axis side travels downstream much faster than that of the long-axis side. As a result, the effect of the separation line jump is split into two parts: the fast moving part of the separation line

associated with the two ends of the short-axis jumps first, and then the slow moving part of the separation line jumps second. This splitting of the separation line jump reduces the peak side load of the significantly out-of-round case to comparable to that of the perfectly round nozzle. The peak side load reduction mechanism of splitting the peak side load physics circumferentially of the significantly out-of-round case agrees with that reported for the non-round, polygon nozzles in the literature. Except for the significantly out-of-round nozzle, the effect of the would-be peak side load physics is split not only in the circumferential direction, but also in time.

Acknowledgments

This study was partially supported by a MSFC J-2X nozzle side load task. The lead author wishes to thank Mike Shadoan for his support of the task and James Back of Pratt-Whitney Rocketdyne for his interest in this task. The fourth co-author wishes to thank Duc Nguyen and Danny Woo of Pratt-Whittney Rocketdyne for providing the engine design and transient sequencing information necessary to create the MSFC J-2X engine system model.

References

[1] Nave, L.H., and Coffey, G.A., "Sea Level Side Loads in High-Area-Ratio Rocket Engines," AIAA Paper 73-1284, Nov. 1973.

[2] Cikanek, H.A., "Characteristics of Space Shuttle Main Engine Failures," AIAA Paper 87-1939, June 1987.

[3] Watanabe, Y., Sakazume, N., and Tsuboi, M., "LE-7A Engine Nozzle Problems During the Transient Operations," AIAA Paper 2002-3841, July 2002.

[4] Shi, J., "Rocket Engine Nozzle Side Load Transient Analysis methodology – A Practical Approach," AIAA Paper 2005 – 1860, April 2005.

[5] Hagemann, G., Terhardt, M., Frey, M., Reijasse, P., Onofri, M., Nasuti, F., and Ostlund, J., "Flow Separation and Side-Loads in Rocket Nozzles," 4th International Symposium on Liquid Space Propulsion, March 12-15, 2000, DLR Lampoldshausen, pp. 1-19.

[6] Ruf, J., McDaniels, D.M., and Brown, A.M., "Nozzle Side Load Testing and Analysis at Marshall Space Flight Center," AIAA Paper 2009-4856, July 2009.

[7] Wang, T.-S., "Transient Three-Dimensional Startup Side Load Analysis of a Regeneratively Cooled Nozzle," *Shock Waves – An International Journal on Shock Waves, Detonations and Explosions.* Vol. 19, Issue 3, 2009, pp. 251~264. DOI: 10.1007/s00193-009-0201-2.

[8] Wang, T.-S., and Guidos, M., "Transient Three-Dimensional Side Load Analysis of a Film-Cooled Nozzle," to appear in *Journal of Propulsion and Power,* Vol. 25, No. 6, 2009. DOI: 10.2514/1.41025.

[9] Ostlund, J., and Bigert, M., "A Sub Scale Investigation Side Loads in Sea Level Rocket Nozzles," AIAA Paper 99-2759, June, 1999.

[10] Ostland, J., "Supersonic Flow Separation with Application to Rocket Engine Nozzles," Doctoral Thesis, Royal Institute of Technology, Stockholm, Sweden, 2004.

[11] Deck, S., "Delayed Detached Eddy Simulation of the End-Effect Regime and Side-Loads in an Overexpanded Nozzle Flow," *Shock Waves – An International Journal on Shock Waves, Detonations and Explosions.* Vol. 19, Issue 3, 2009, pp. 239~249. DOI: 10.1007/s00193-009-0199-5.

[12] Hadjada, A., and Onofri, M., "Nozzle Flow Separation," *Shock Waves – An International Journal on Shock Waves, Detonations and Explosions.* Vol. 19, Issue 3, 2009, pp. 163~169. DOI: 10.1007/s00193-009-0209-7.

[13] Tomita, T., Takahashi, M., Sasaki, M., Sakamoto, H., Takahashi, M., Tamura, H., "Experimental Evaluation of Side Loads in LE-7A Prototype Engine Nozzle," *Shock Waves – An International Journal on Shock Waves, Detonations and Explosions.* Vol. 19, Issue 3, 2009, pp. 213~228. DOI: 10.1007/s00193-009-0191-0.

[14] Nguyen, A.T., Deniau, H., Girard, S., and De Roquefort, T.A., "Unsteadiness of Flow Separation and End-Effects Regime in a Thrust-Optimized Contour Rocket Nozzle," Flow, Turbulence and Combustion, Vol. 71, 2003, pp.161-181.

[15] Deck S., and Guillen, P., "Numerical Simulation of Side loads in an Ideal Truncated Nozzle," *Journal of Propulsion and Power,* Vol. 18, No. 2, 2002, pp. 261-269.

[16] Shimizu, T., Miyajima, H., and Kodera, M., "Numerical Study of Restricted Shock Separation on a Compressed Truncated Perfect Nozzle," *AIAA Journal*, Vol. 44, No. 3, 2006, pp. 576-584.

[17] Kwan, W., and Stark, R., "Flow Separation Phenomena in Subscale Rocket Nozzles," AIAA Paper 2002-4229, July 2002.

[18] Reijasse, Ph., and Boccaletto, L., "Influence of Film Cooling on Nozzle Side loads," AIAA Paper 2008-392, Jan. 2008.

[19] Wang, T.-S., "Multidimensional Unstructured-Grid Liquid Rocket Engine Nozzle Performance and Heat Transfer Analysis," *Journal of Propulsion and Power,* Vol. 22, No. 1, January-February, 2006, pp. 78-84.

[20] Shang, H.M., and Chen, Y.-S., "Unstructured Adaptive Grid method for Reacting Flow Computation," AIAA Paper 1997-3183, July 1997.

[21] Wang, T.-S., Chen, Y.-S., Liu, J., Myrabo, L.N., and Mead, F.B. Jr., "Advanced Performance Modeling of Experimental Laser Lightcraft," *Journal of Propulsion and Power,* Vol. 18, No. 6, 2002, pp. 1129-1138.

[22] Chang, G., Ito, Y., Ross, D., Chen. Y.-S., Zhang S., and Wang, T.-S., "Numerical Simulations of Single Flow Element in a Nuclear Thermal Thrust Chamber" AIAA Paper 2007-4143, June 2007.

[23] Chen, Y.-S., and Kim, S. W., "Computation of Turbulent Flows Using an Extended k-ε Turbulence Closure Model," NASA CR-179204, Oct. 1987.

[24] Wang, T.-S., Droege, A., D'Agostino, M., Lee, Y.-C., and Williams, R., "Asymmetric Base-Bleed Effect on X-33 Aerospike Plume Induced Base-Heating Environment," *Journal of Propulsion and Power,* Vol. 20, No. 3, 2004, pp. 385-393.

[25] Chen, Y.-S., Cheng, G.C., and Farmer, R.C., "Reacting and Non-Reacting Flow Simulation for Film Cooling in 2-D Supersonic Flows," AIAA Paper 92-3602, July 1992.

[26] Wang, T.-S., Canabal, F., Chen, Y.-S., and Cheng, G.C., "Multiphysics Computational Analysis of a Solid-Core Nuclear Thermal Engine Thrust Chamber," *Journal of Propulsion and Power,* Vol. 26, No. 3, May-June, 2010, pp. 407-414.

[27] Svehla, R.A., and McBride, B.J., "FORTRAN IV Computer Program for Calculation of Thermodynamic and Transport Properties of Complex Chemical Systems," NASA TN D-7056, Jan. 1973.

[28] Steinbrenner, J.P., Chawner, J.R., and Fouts, C., "Multiple Block Grid Generation in the interactive Environment," AIAA Paper 90-1602, June 1990.

[29] Tomita, T., Takahashi, M., Sasaki, M., Takahashi, M., Tamura, H., Watanabe, Y., and Tsuboi, M., " Parametric Study on the Influence of a Discontinuous Step in a Nozzle Contour on Side-Load," AIAA Paper 2003-4764, July 2003.

[30] Wonezawa, K., Yokota, K., Tsujimoto, K., Sakazume, N., and Watanabe, Y., "Three-Dimensional Unsteady Flow Simulation of Compressed Truncated Perfect nozzles," AIAA Paper 2002-3991, July 2002.

[31] Coanda, H., "Device for Deflecting a Stream of Elastic Fluid Projected into an Elastic Fluid," US Patent # 2,052,869, Sept. 1, 1936.

Transient Three-Dimensional Side Load Analysis of Out-of-Round Film Cooled Nozzles

Ten-See Wang, Jeff Lin, and Joe Ruf

CFD Team, Fluid Dynamics Branch

Propulsion Structure, Thermal, and Fluids Analysis Division

Mike Guidos

Liquid Engine and Main Propulsion System Branch

Propulsion System Design and Integration Division

NASA – Marshall Space Flight Center

MSFC, AL 35812

July 25-28, 2010

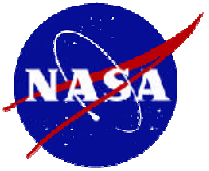

Outline

- Introduction
- Introduction of J-2X Engine
- Side Loads and Motivations
- Objective
- Transient 3D Nozzle Side Load Computational Methodology
- Coanda Effect
- Strong Driving Factors on Side Load Physics
- Strategies in Modeling
- Benchmark with the Regeneratively Coold SSME nozzle during Sea Level Startup
- Comparison of J-2X Sea Level Results with those of LE-7A
- Run Matrix
- Computational Grid Layout for Round Nozzle
- Top View of the Four Ovalized Nozzles
- Transient Startup Inlet Flow Properties (System Model Rev. 3.5)
- Asymmetric TEG Pumping
- Computed Side Load Histories for the Out-of-Round Cases
- Ostlund and Bigert test's Sea Level Test of polygon nozzles
- Summary

Introduction

- Nozzle side loads are detrimental to the engine components such as actuator, cooling tubes, propellant feed lines, .., etc. for almost all rocket engines during development.
- Past failures during sea level testing
  - J-2 engine had its gimbal block retaining bolt failed in tension
  - Space Shuttle Main Engine (SSME) had the liquid H2 feedline or steerhorn fractured from low cycle fatigue during the shutdown transient
  - Japanese LE-7A engine had its cooling tubes broken
- Past failure during flight
  - During its maiden flight, the European Vulcain engine overheated due to a leak developed in cooling pipes

J-2

SSME

LE-7A

Vulcain

Introduction of J-2X Engine

- J-2X engine, the Ares I upper stage engine under development, is an evolved variation of two historic predecessors: the J-2 and J-2S engines.
- In addition, there is a common feature shared by 3 current engines, J-2X, LE-7A, and Vulcain: turbine exhaust gas (TEG) is used to boost the thrust and cool the nozzle extension.
- As a result, J-2X engine will develop nozzle side load during the transient startup and shutdown processes.

J-2X

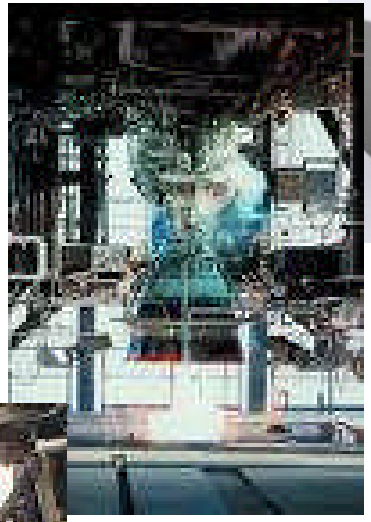

LE-7A

Vulcain 2

SSME Hot Firings

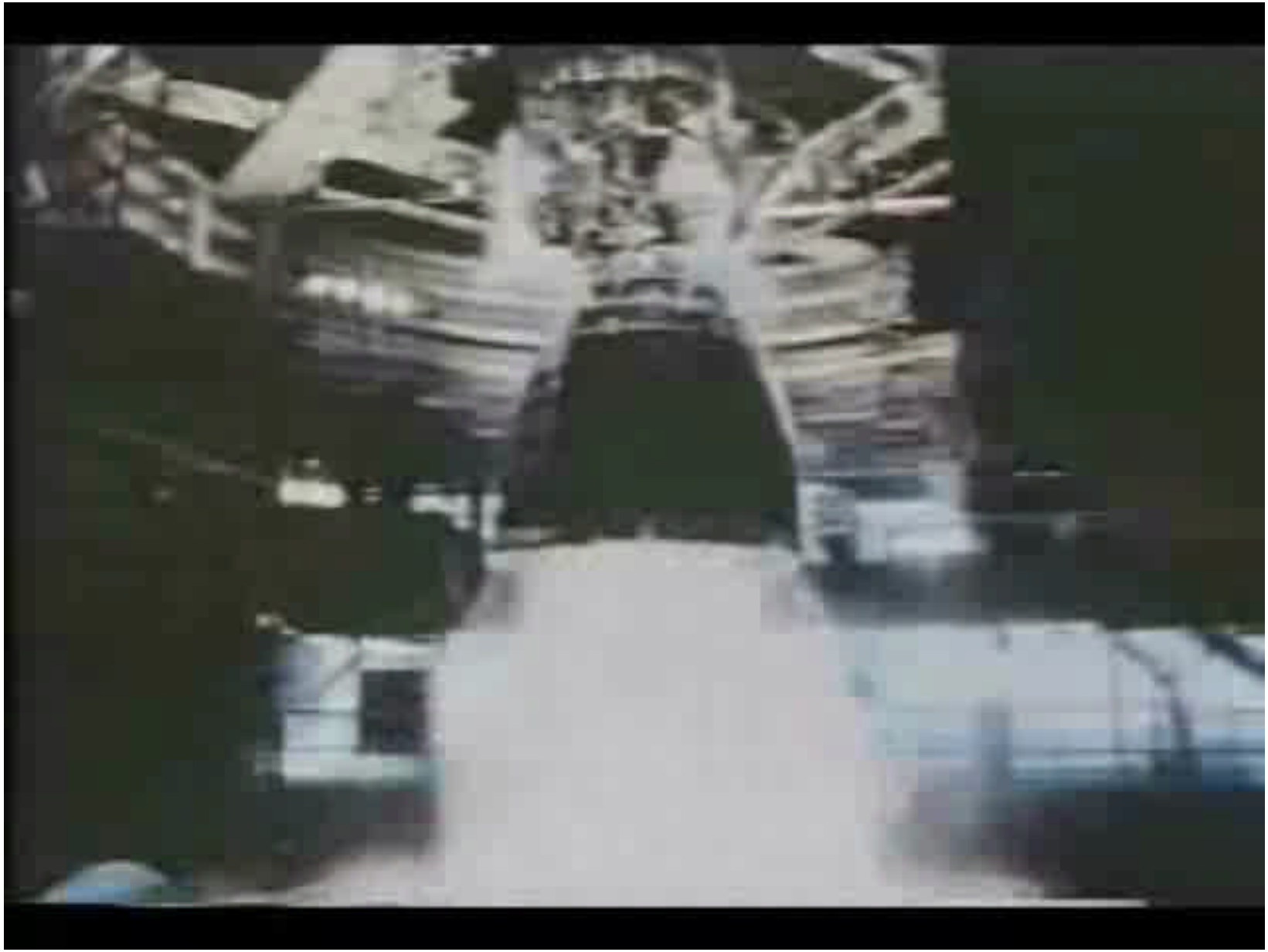

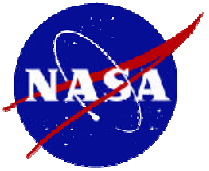

Side loads and Motivations

- Side forces are caused by asymmetric (3D) shock physics in the nozzle during the transient engine startup and shutdown processes.
- Side load is the most important design parameter during the design process
- Since asymmetric shock revolutions inside the nozzle generate side loads naturally on perfectly round nozzles, questions were raised about the side load characteristics of out-of-round nozzles.
- Liquid rocket engine nozzles, being large with relatively light weight structures, are probably never truly round. The cause of out-of-roundness could be, but are not limited to, the following:
  - asymmetric loads induced by hardware attached to the nozzle
  - asymmetric material internal stresses induced in previous tests or nozzle wall material deformation, such as creep, incurred in previous engine tests

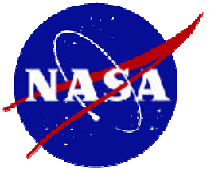

Objective

- To investigate the effect of nozzle out-of-roundness on the start transient side loads.
  - Since J-2X is an upper stage engine and the tests will be performed in an altitude test stand that provides a simulated altitude of 100,000 ft, transient 3-D CFD computations were performed for the engine startup with a back pressure equivalent to 100,000 ft.
  - Four nozzles with different degrees of ovalization were used to study the effect of out-of-roundness: a perfectly round nozzle or the baseline nozzle, a slightly ovalized nozzle, a more ovalized nozzle, and a significantly ovalized nozzle.

Transient 3-D Nozzle Side Load Computational Methodology

- Multidisciplinary computational methodology
  - UNIC time-accurate, unstructured-grid, pressure-based, reacting flow, CFD & heat transfer code
  - Engine system modeling for transient inlet properties (to simulate hot-firing tests)
  - Thermal modeling of wall temperatures for combustion chamber, nozzle, and nozzle extension (to simulate hot-firing tests)

Coanda Effect

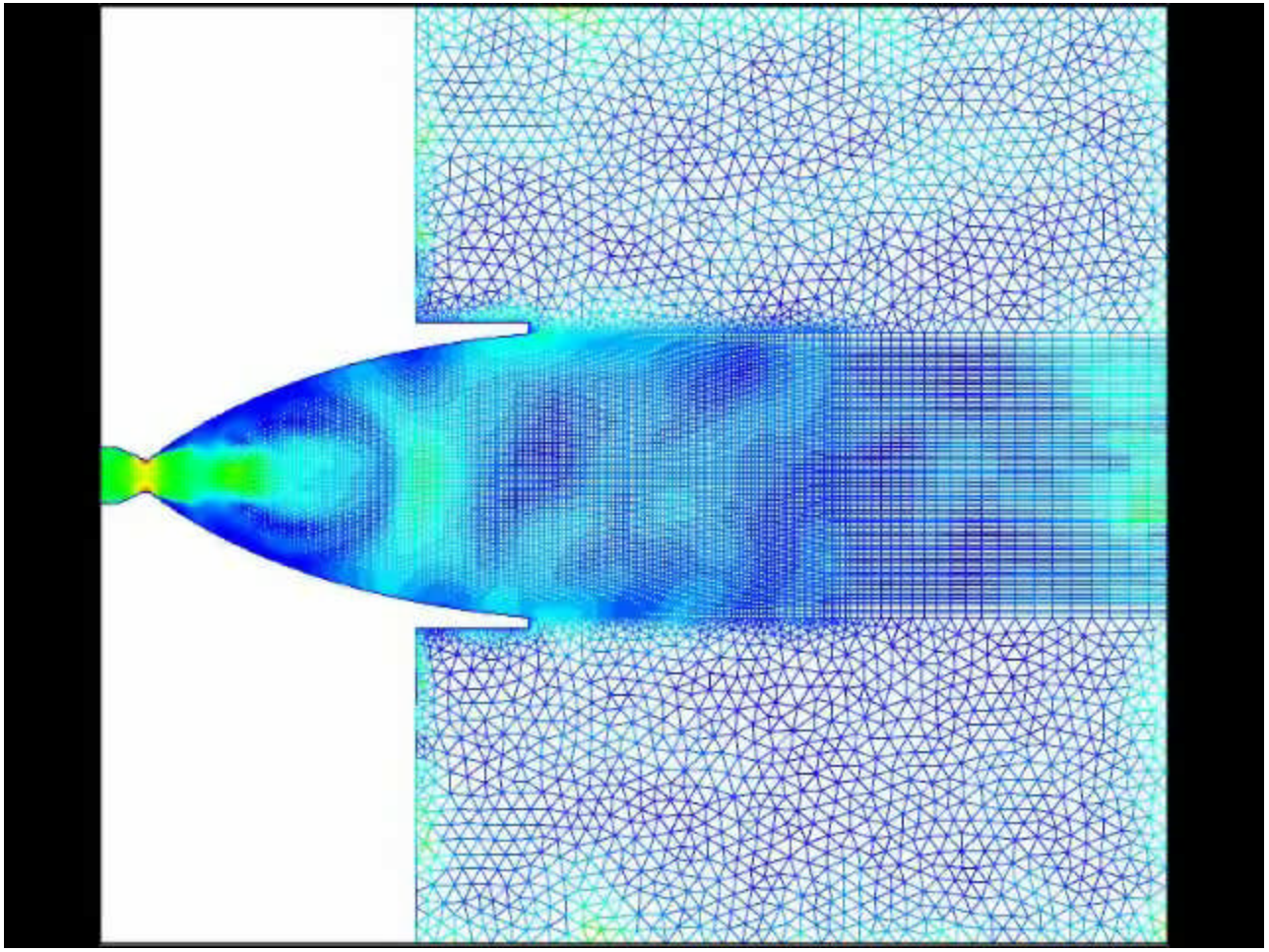

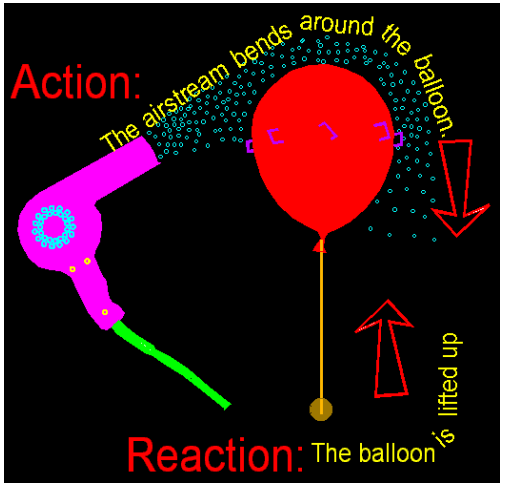

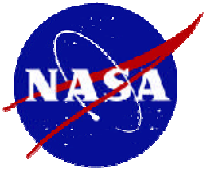

Strong Driving Factors on Side Load Physics

- Residence times
  - Transient flows – Inlet conditions come from system modeling (short ramp time decreases side loads)
  - Reacting flows – finite-rate chemistry (sea level environment results in longest residence time, strongest combustion, largest side loads)
- Boundary conditions
  - Wall temperatures – thermal modeling (regeneratively cooled wall promotes RSS formation, thereby large side loads)
  - Aeroelastic motions

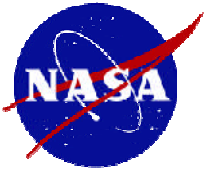

Strategies in Modeling

- Grid study to match axial force and capture Mach disk during full flow condition
- Benchmark or comparing results with available, actual rocket engine hot-firing
  - Benchmarked with a regeneratively cooled engine – SSME (side load physics to be captured: combustion wave, FSS-to-RSS and RSS-to-FSS transitions, cold wall promoted Coanda effect, RSS shock breathing)
  - Compared J-2X sea level results with another film cooled engine – LE-7A (side load to be captured: separation line jump)

Benchmark with the Regeneratively Coold SSME nozzle during Sea Level Startup

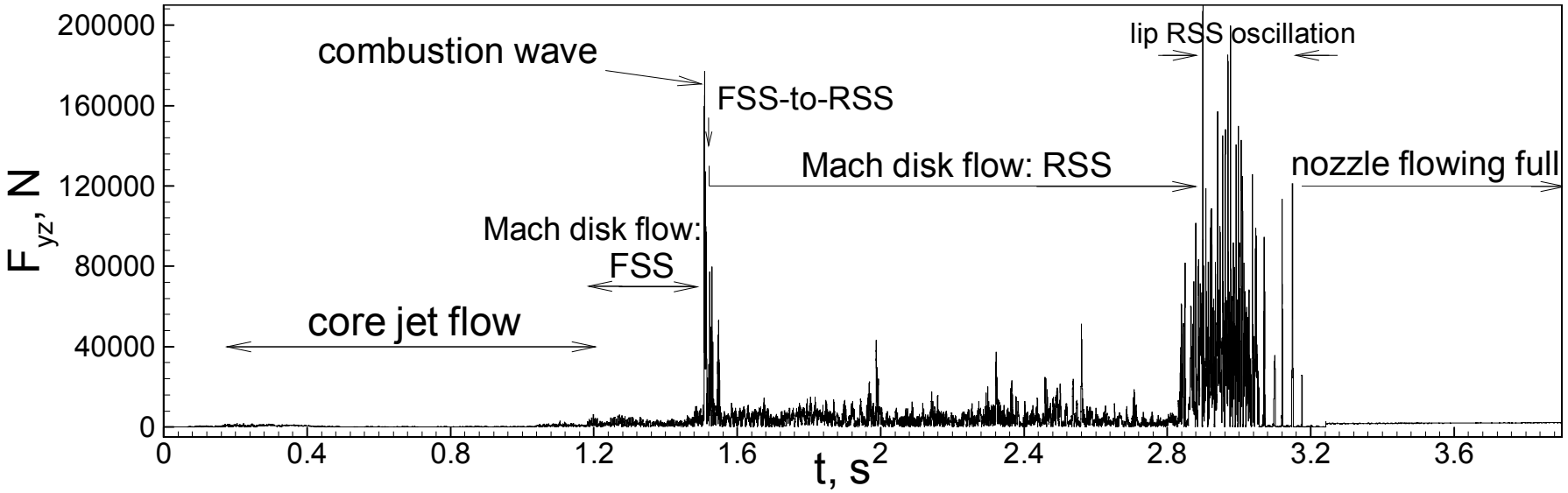

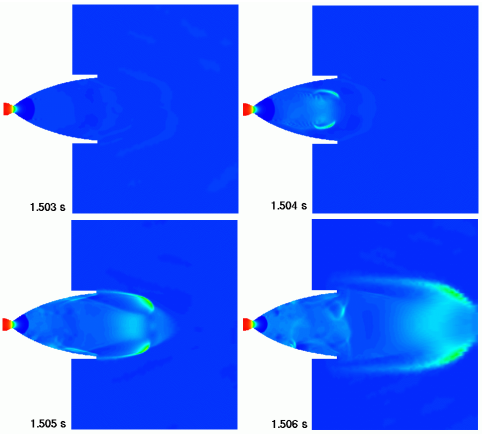

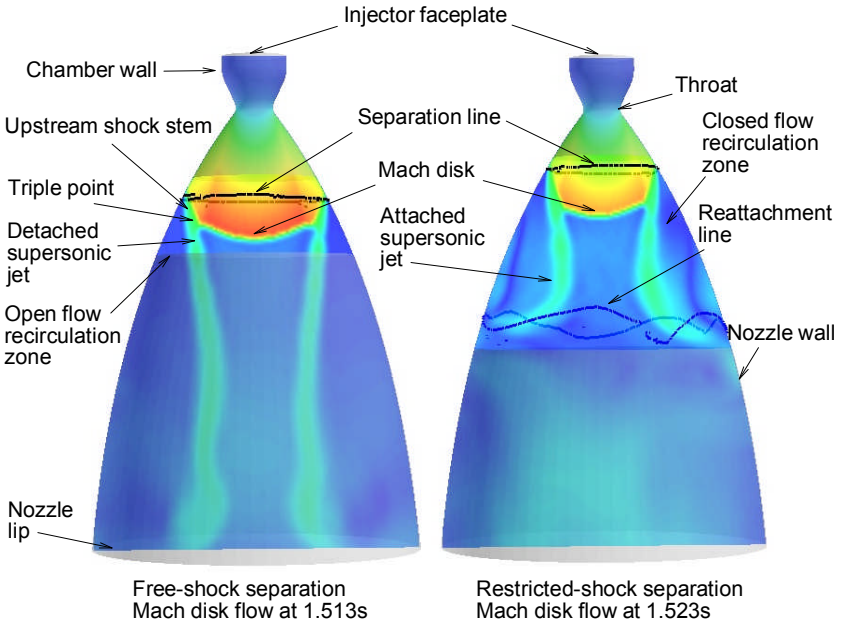

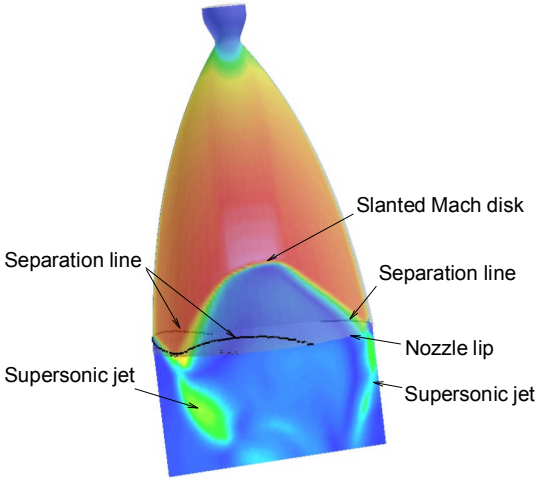

A Comparison of Dominant Frequencies during Shock Breathing across the Lip

	Dominant frequency, Hz	Variable
Adiabatic nozzle	45	pressure
	49	temperature
Cooled nozzle	122	pressure
	125	heat flux
Test	125	

A comparison of local peak side loads

F_{yz}, kN	Test	Computation		
		Adiabatic nozzle	**Cooled nozzle**	physics
-	-	395	176	Combustion wave
1st peak	**90***	70	**80**	FSS-to-RSS transition
		102	-	RSS-to-FSS transition
2nd peak	**200***	110	-	FSS-to-partial RSS transition
		60	-	FSS breathing across lip
		-	**212**	RSS breathing across lip

* Normalized.

Comparison of J-2X Sea Level Results with those of LE-7A

- Watanabe's LE-7A hot-fire Tests at sea level (Watanabe, Yasuhide, et al., "LE-7A Engine Nozzle Problems during the Transient Operations," AIAA Paper 2002-3841).
  - He measured the transient side loads of LE-7A engine with and without the nozzle extension, and found out the side load of the stub nozzle reduced drastically.

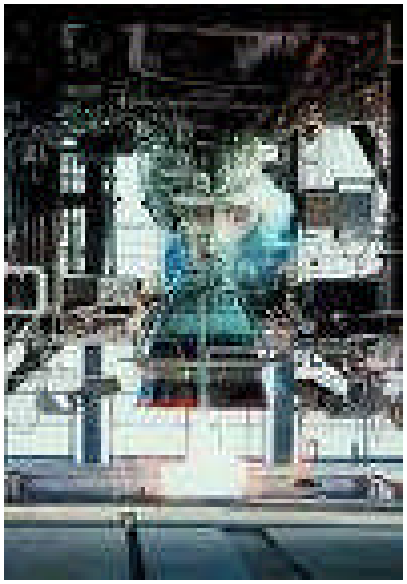

Peak Side Load Physics for Film Cooled Engines

TEG film coolant induced asymmetric Mach disk flow and the subsequent jump of the separation line that generated the peak side load at 61k ft

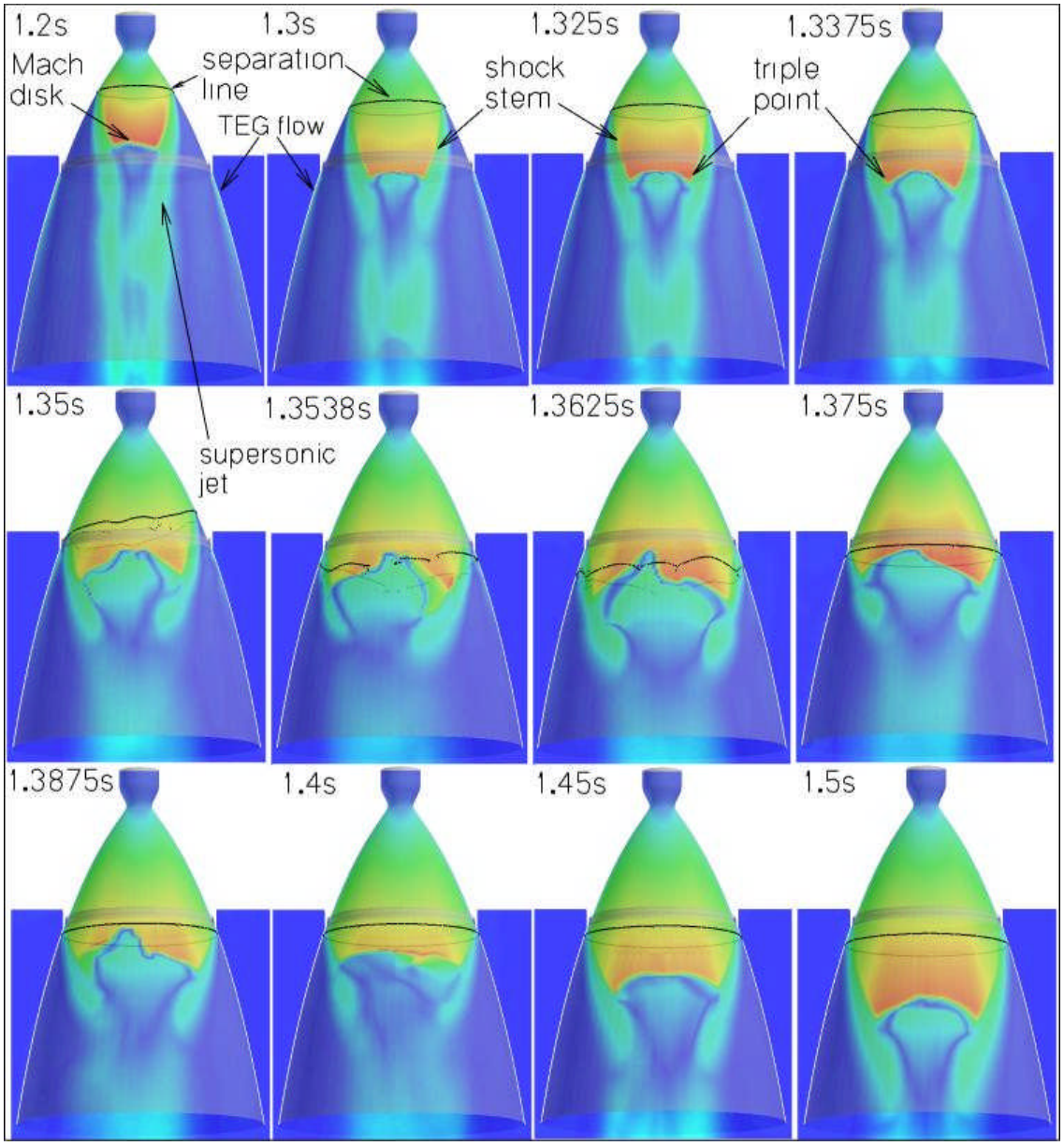

Comparison of Computed J-2X (Nozzlette) Nozzle Side Loads at Sea Level With those of LE-7A Hot-Fire Test

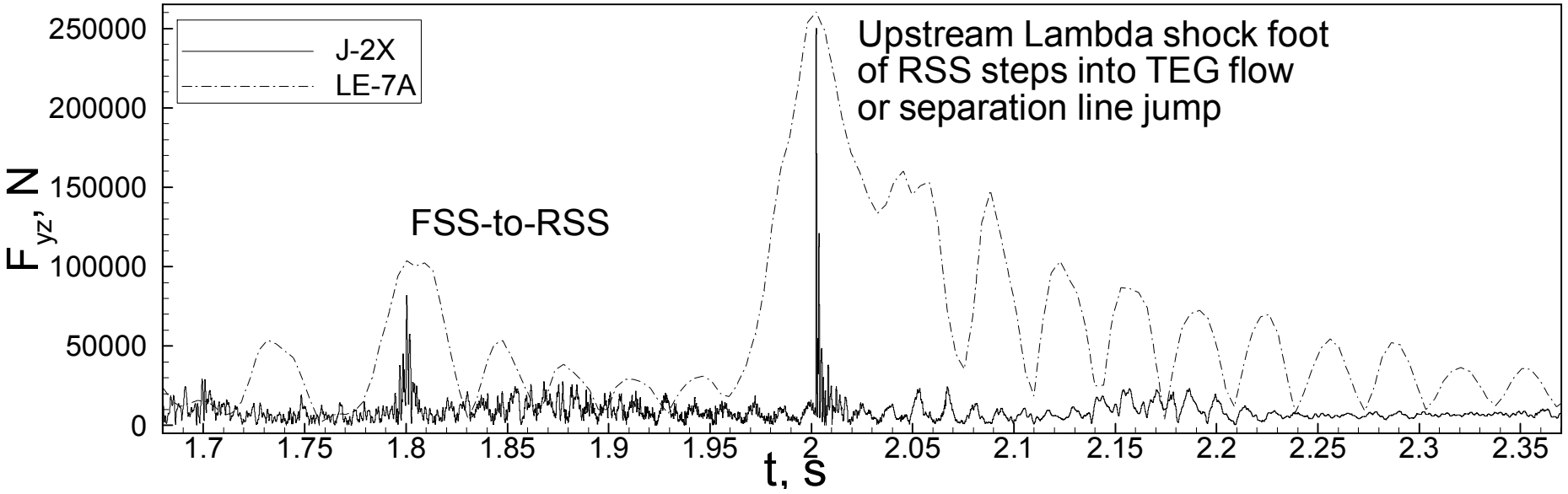

A Comparison of the Sea Level Peak Side Loads between J-2X and LE-7A

Side load, kN		J-2X	LE-7A	physics
With extension	1st peak	80	102	Shock transition
	2nd peak	249	259	Separation line jumping
Without extension	1st peak	26	45	Shock transition & breathing
	2nd peak	-	-	

Run Matrix

Case	Description	L/S
1	Nominal or perfectly round	1.0000
2	Slightly out-of-round	1.0086
3	More out-of-round	1.0346
4	Significantly out-of-round	1.4400

Computational Grid Layout for Round Nozzle

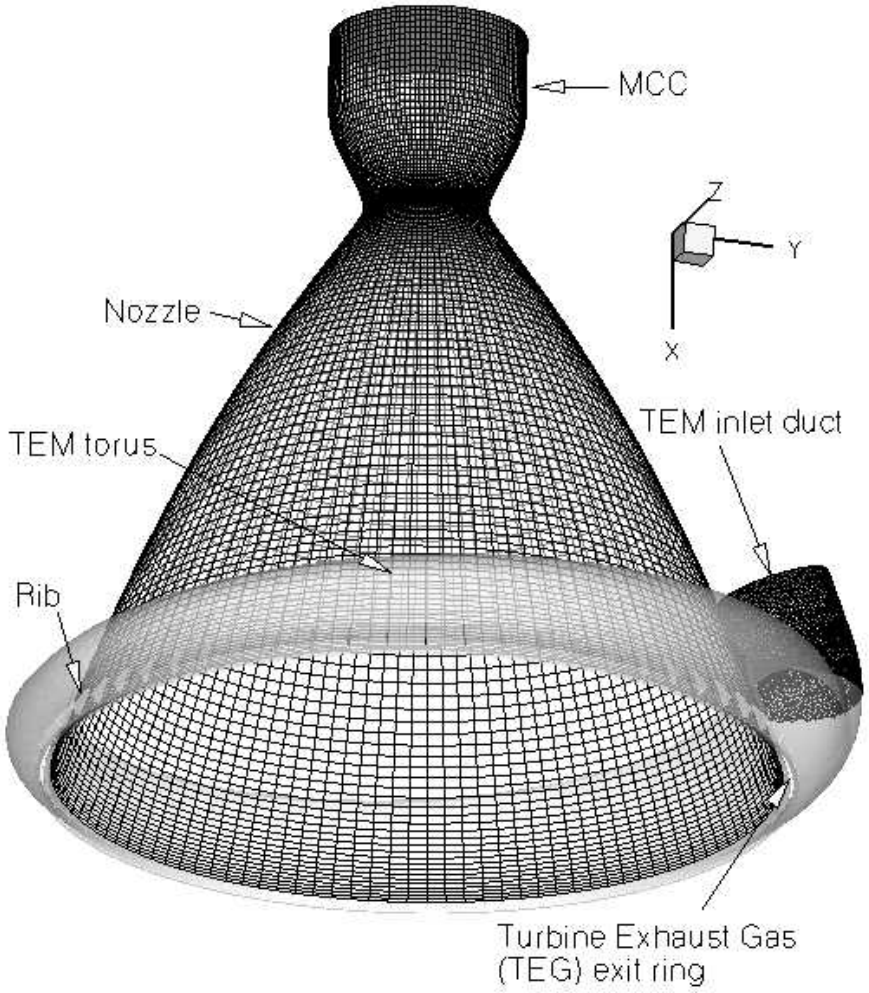

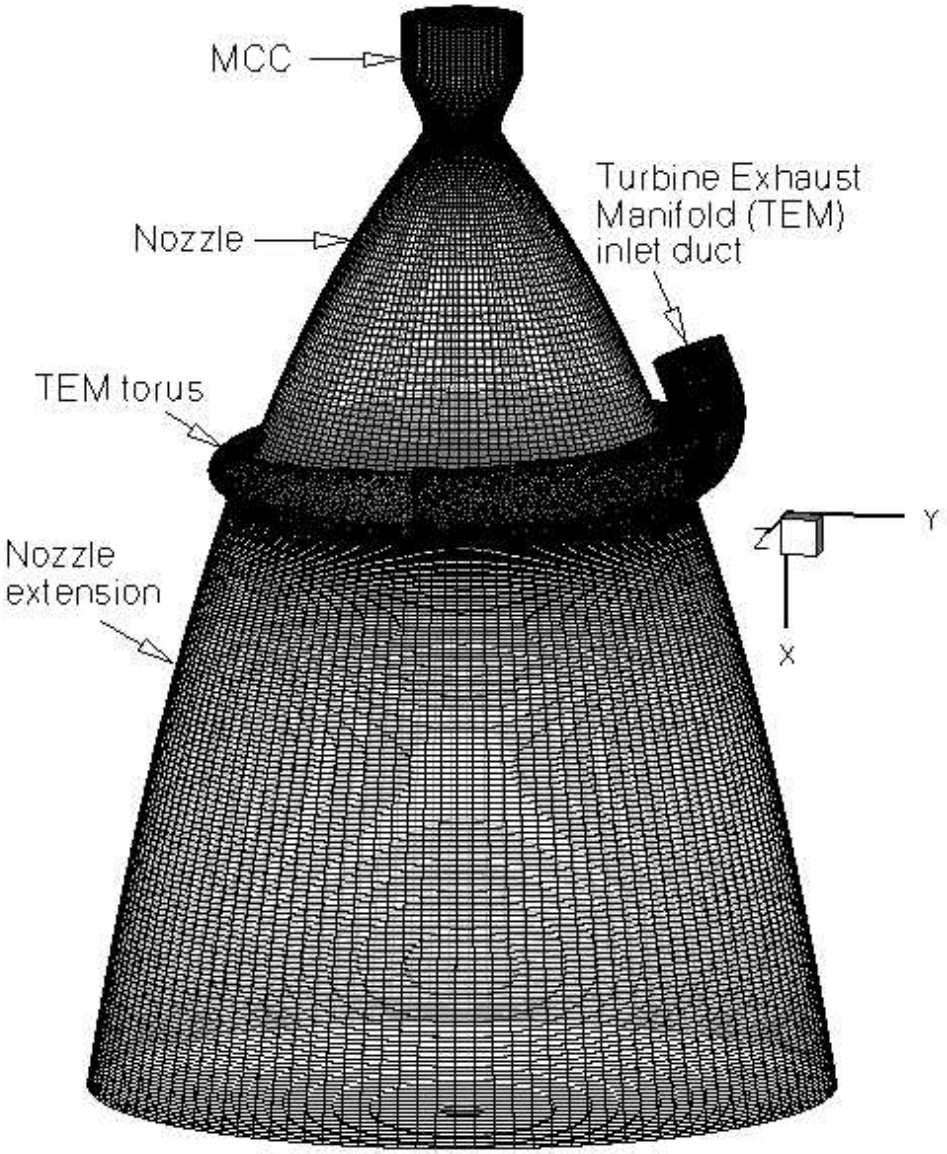

Teepees Captured during Shock Breathing Mode with the Round Stub Nozzle

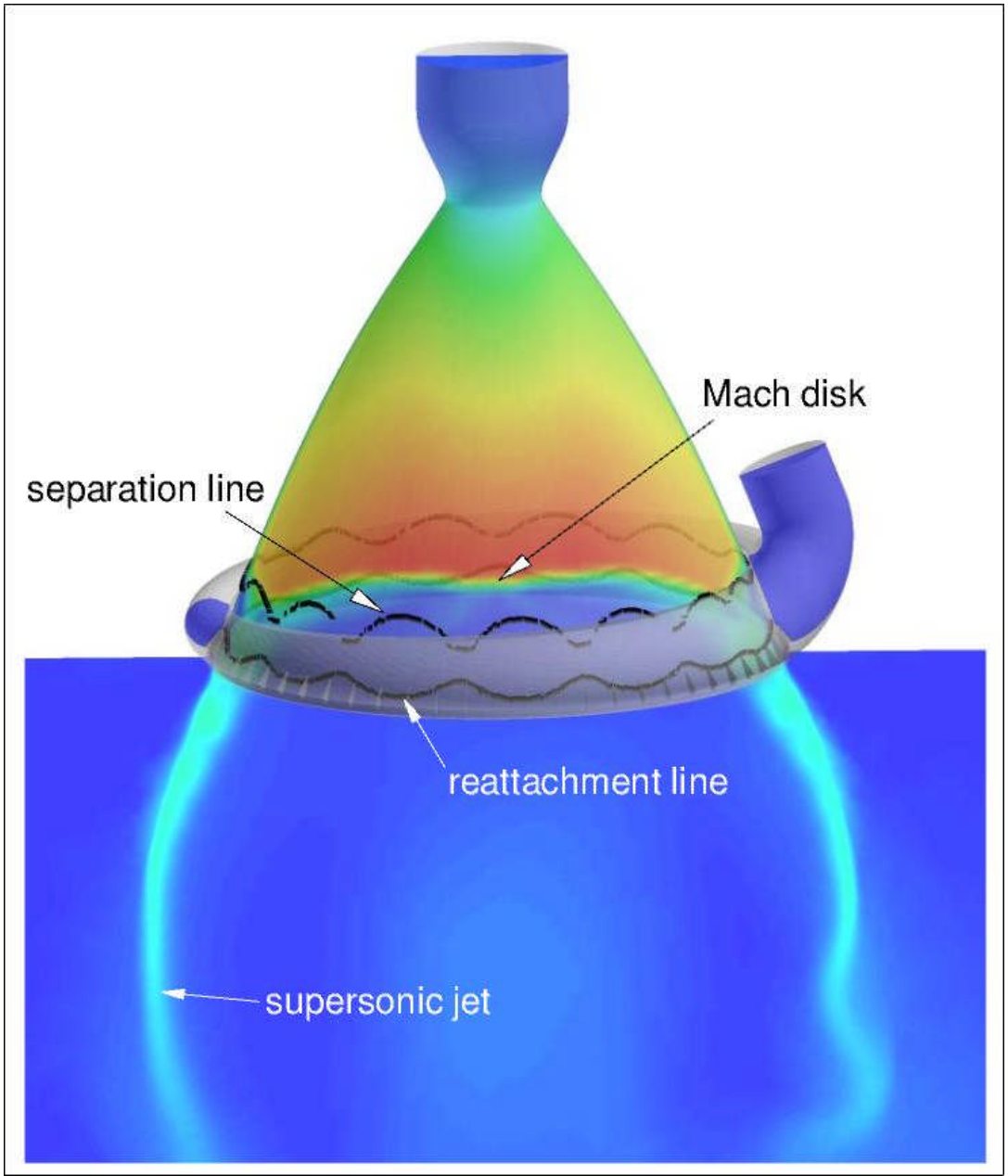

Top View of the Four Ovalized Nozzles

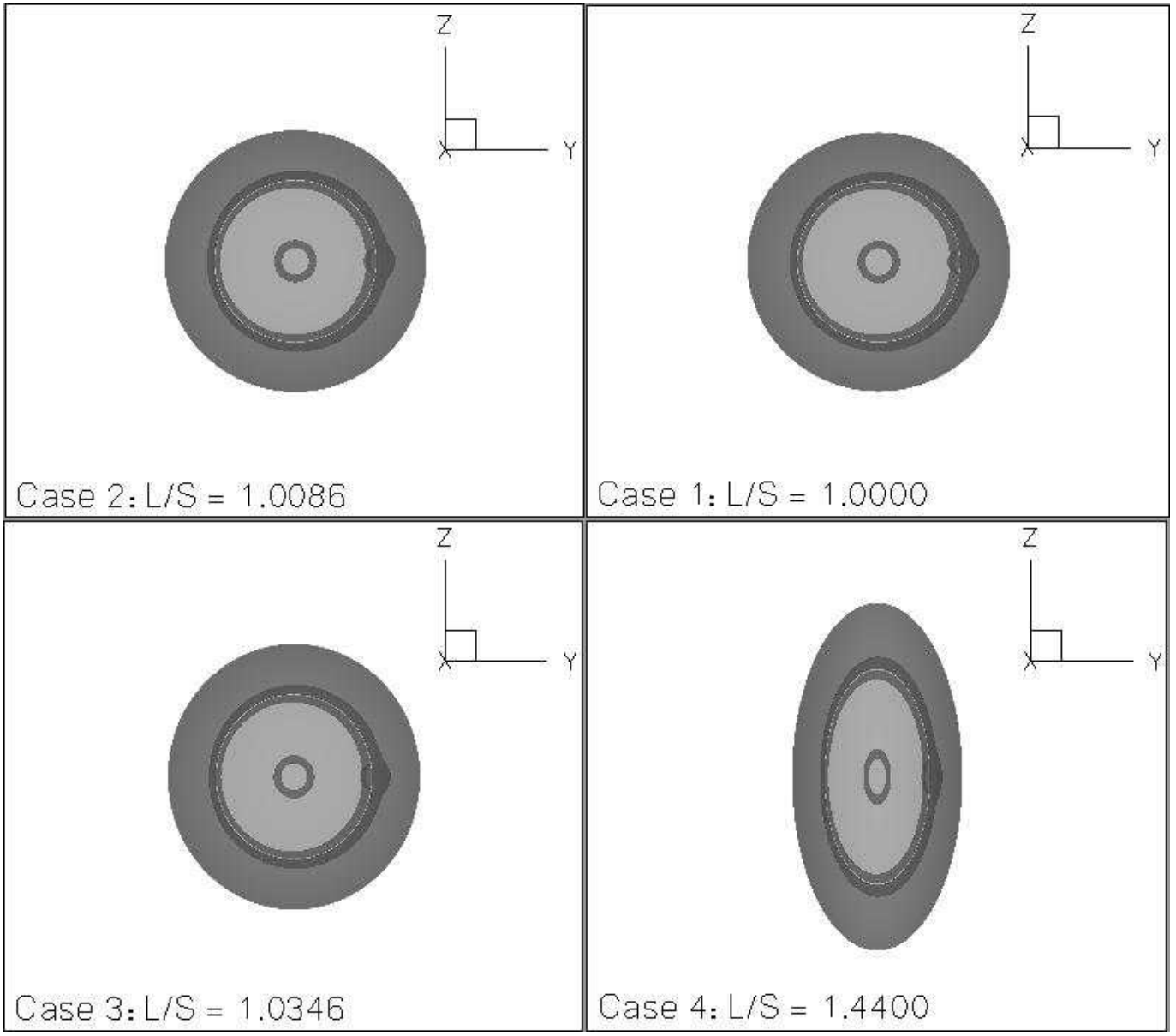

Transient Startup Inlet Flow Properties (System Model Rev. 3.5)

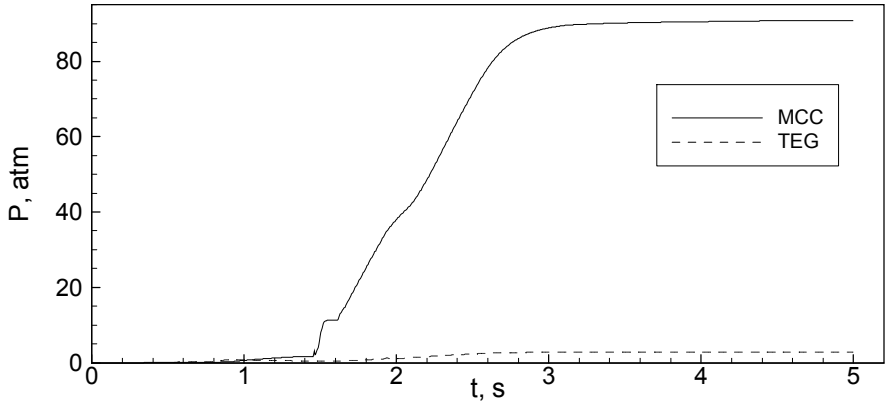

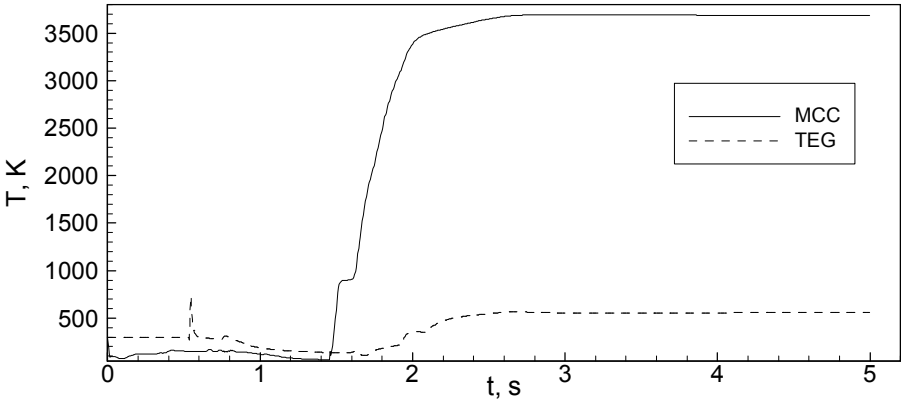

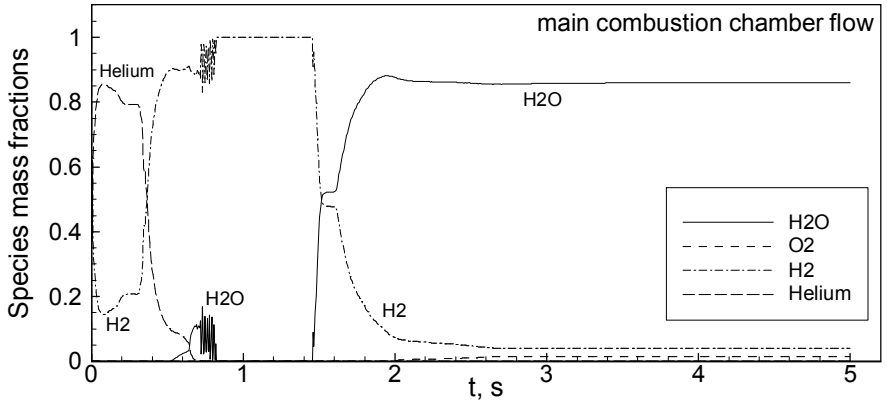

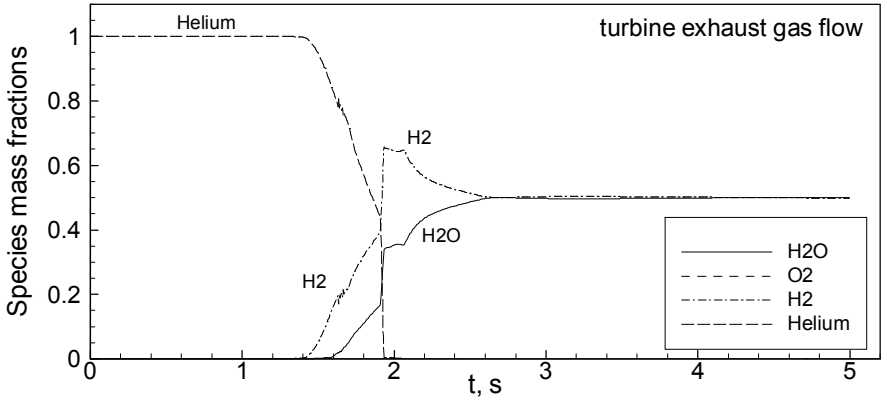

Mach Number Contours for the Nominal Case

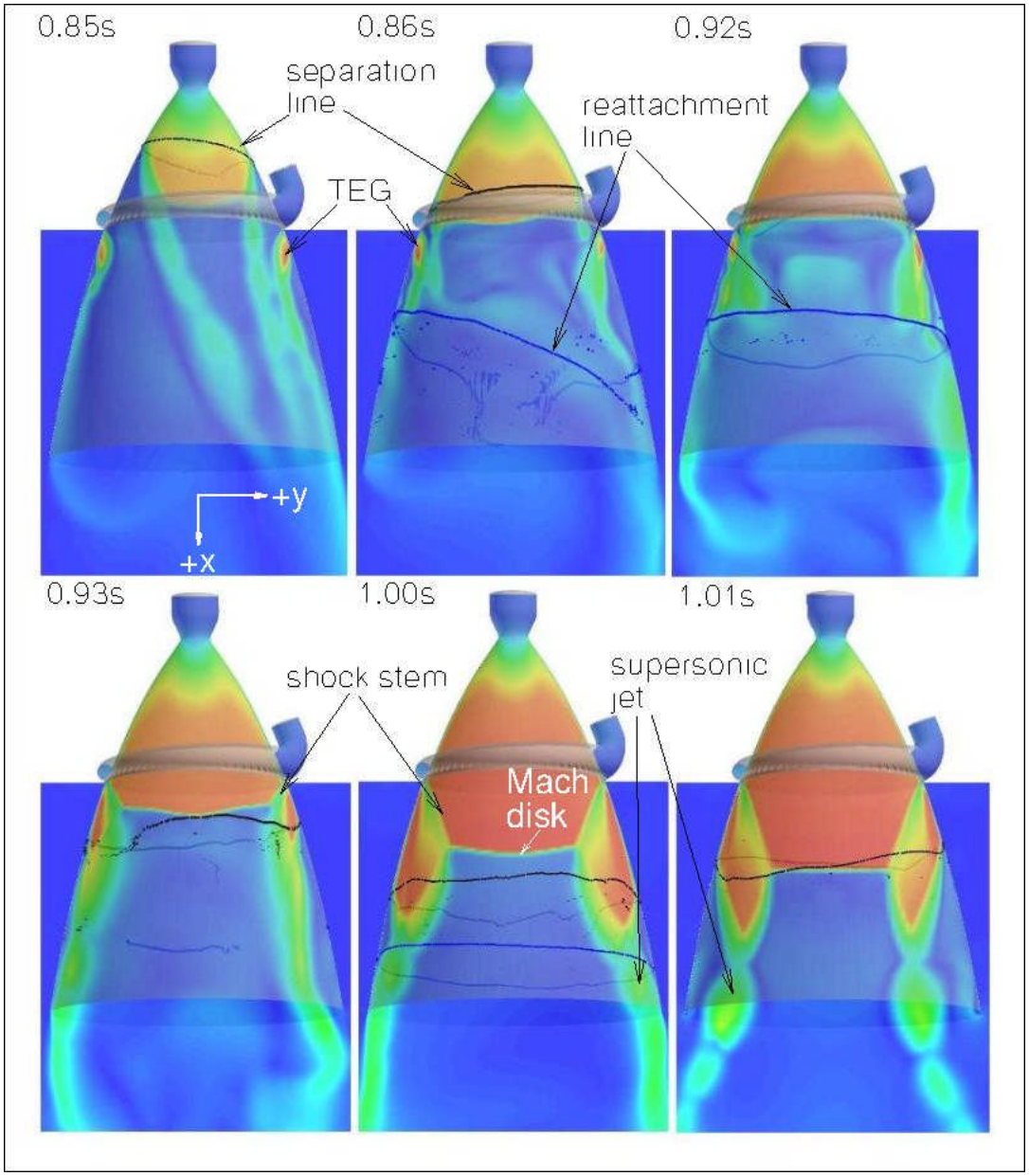

Computed Side Load Histories for the Nominal Case

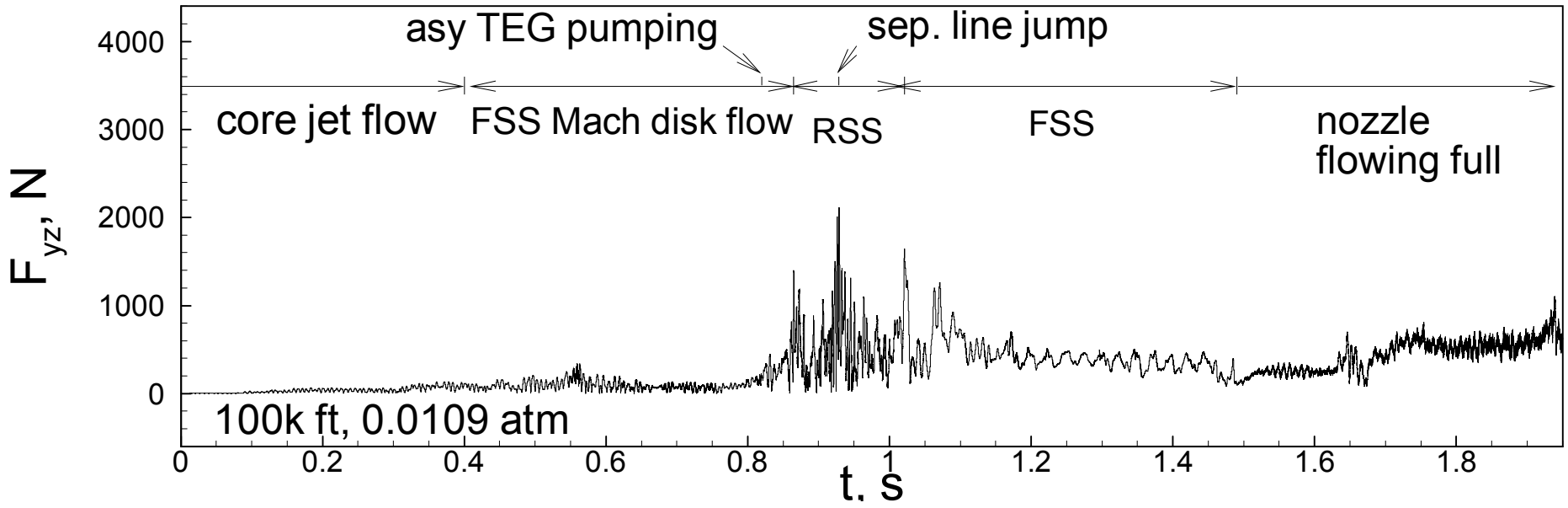

Computed Side Load Histories for the Slightly Out-of-Round Case

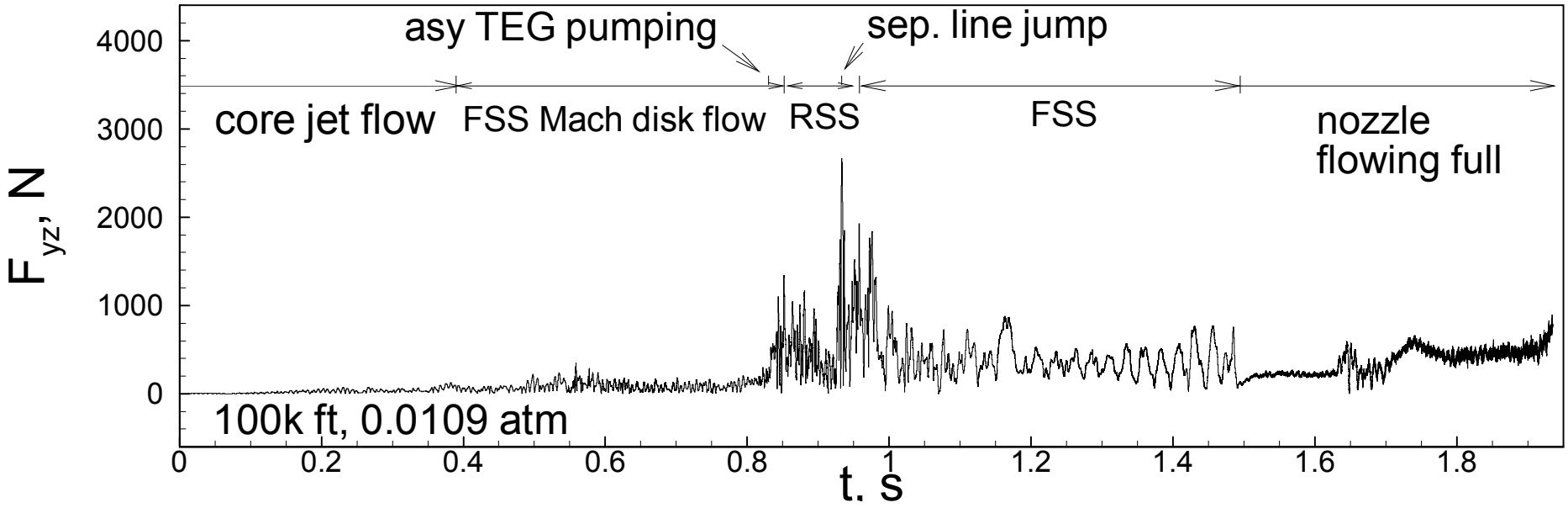

Mach Number Contours for the More Out-of-Round Case

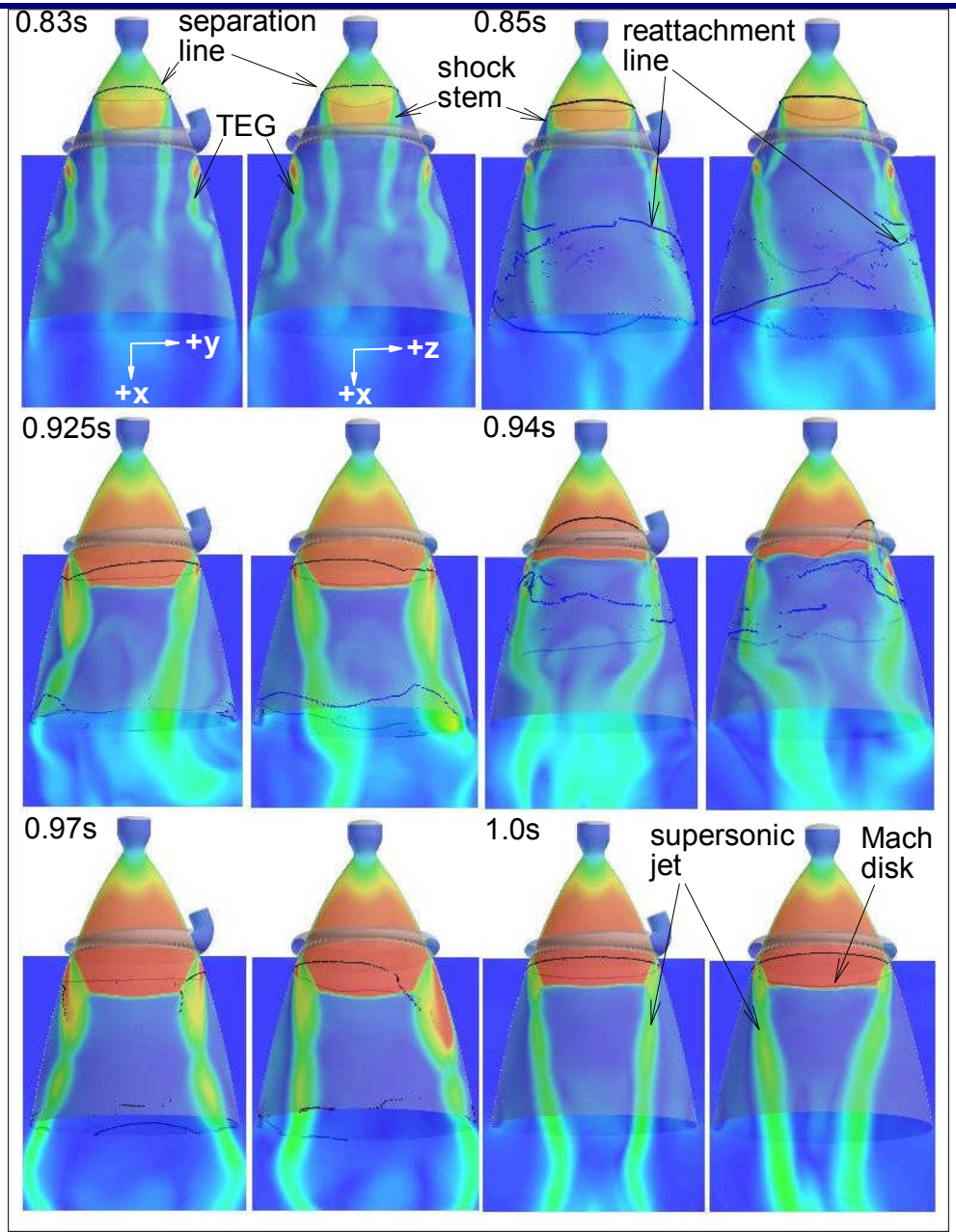

Computed Side Load Histories for the More Out-of-Round Case

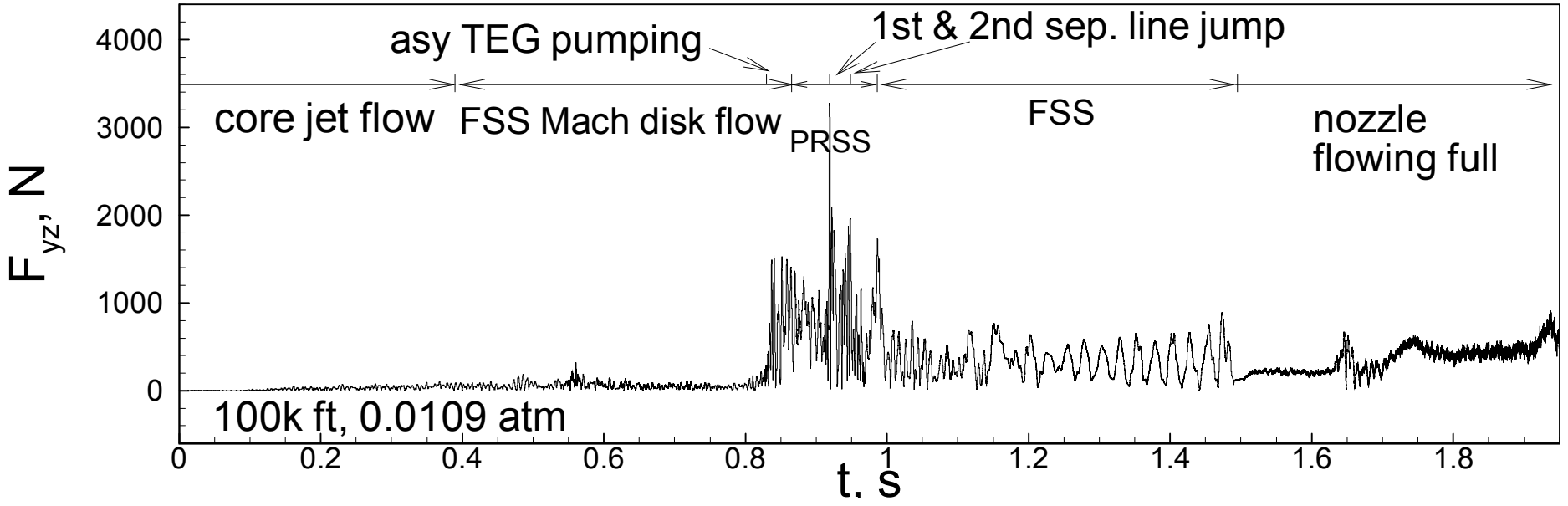

Computed Side Load Histories for the Significantly Out-of-Round Case

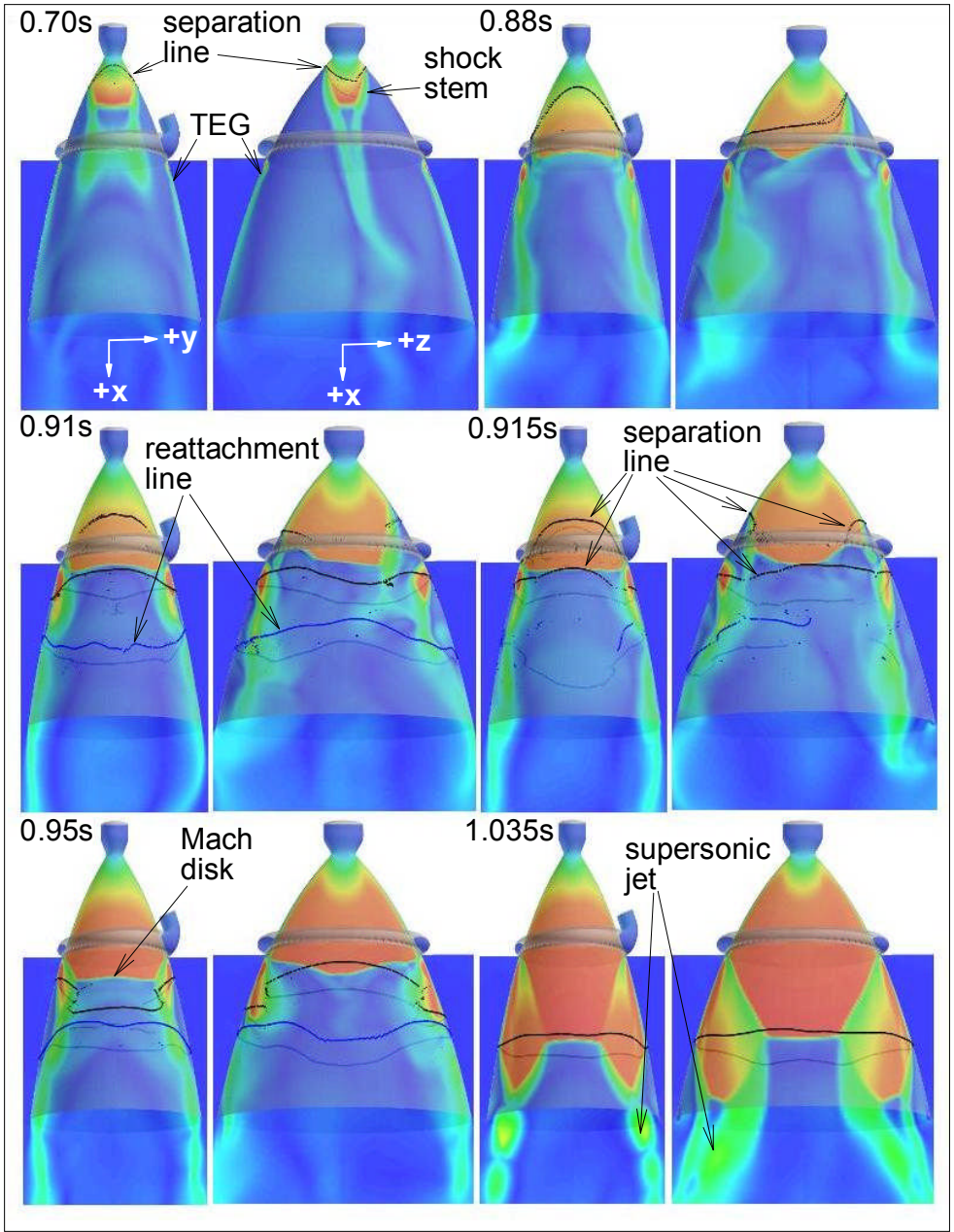

Computed Side Load Histories for the Significantly Out-of-Round Case

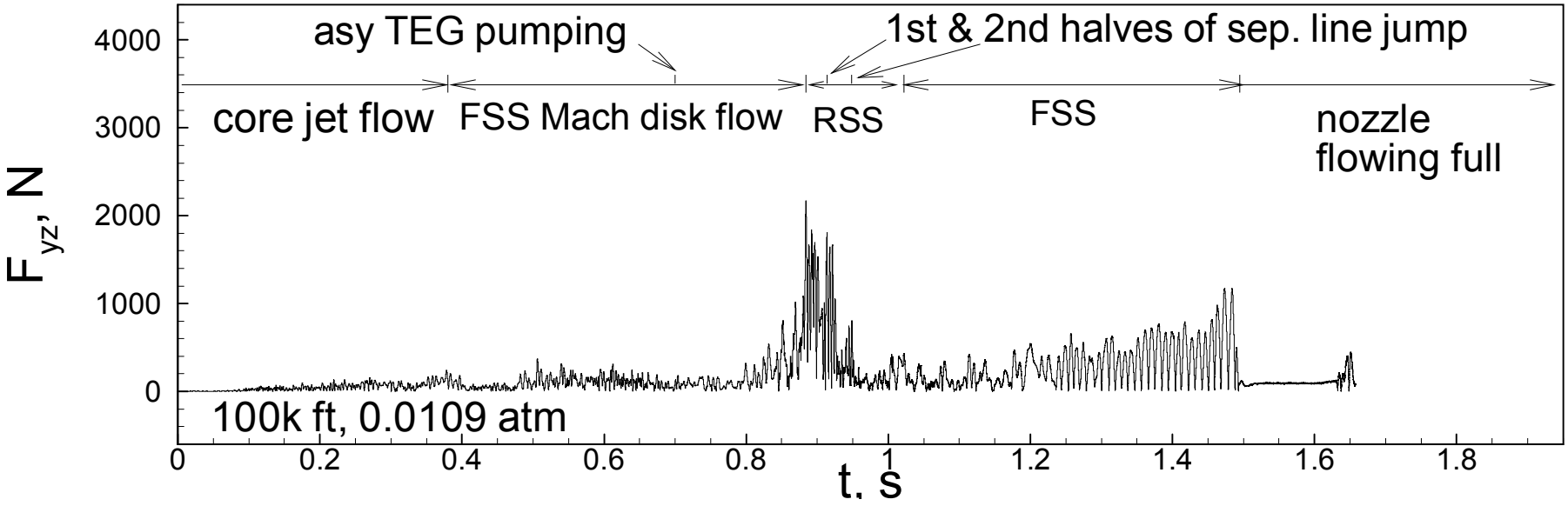

A Comparison of the Computed Peak Side Loads

Nozzle shape	Peak Fyz, N	Physics
Perfeectly round	2114	Separation line jump
Slightly our-of-round	2668	Separation line jump
More out-of-round	3275	Separation line jump
Significantly out-of-round	2171	FSS-to-RSS transition

Ostlund and Bigert test's Sea Level Test of polygon nozzles

- Ostlund & Bigert, "A Sub Scale Investigatinon Side Loads in Sea Level Rocket Nozzles," AIAA Paper 99-2759.
  - Designed polygon nozzles with 7 to 11 sides to reduce peak side load from FSS-to-RSS transition for Vulcain nozzles.
  - the polygon corners act as a kind of structure-breaker, leading to splitting of the separation of the flow pattern in the circumferential direction.

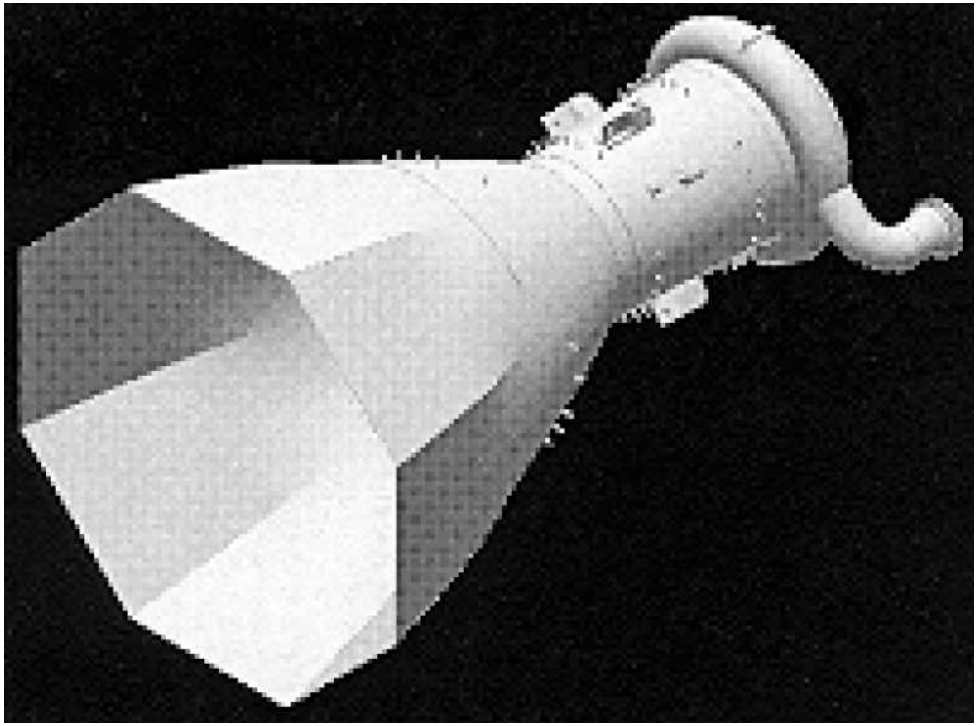

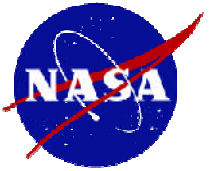

Summary

- Peak side load physics for the round, slightly our-of-round, and more out-of-round cases is the separation line jump, and the peak side load increases as the degree of out-of-roundness increases.
- For the significantly out-of-round case, a surprising flow stabilizing effect is discovered. That flow stabilizing effect is caused by a combination of the highly stretched long-axis to short-axis ratio and the Coanda effect. The separation line on the two ends of short-axis side travels downstream much faster than those of the long-axis side. As a result, the separation line jump is split into two parts: the fast moving part of the separation line associated with the short-axis jumps first, and then the slow moving part of the separation line jumps second. This splitting of the separation line jump reduces the peak side load of the significantly out-of-round case to comparable to that of the round nozzle.